https://doi.org/10.5194/acp-2021-404
Preprint. Discussion started: 15 June 2021

Atmospheric Chemistry and Physics Discussions

Evaluation of modeled summertime convective storms using polarimetric radar observations

Prabhakar Shrestha[1], Silke Trömel[1,2], Raquel Evaristo[1], and Clemens Simmer[1]

[1]Institute of Geosciences, Meteorology Department, Bonn University, Germany
[2]Laboratory for Clouds and Precipitation Exploration, Geoverbund ABC/J, Bonn, Germany

Correspondence: Prabhakar Shrestha (pshrestha@uni-bonn.de)

Abstract. Ensemble simulations were conducted for three summertime convective storms over a temperate region in north-western Germany using the Terrestrial Systems Modeling Platform (TSMP). The simulated microphysical processes were evaluated with polarimetric observations from two X-band radars, with the help of a forward operator applied to the model data. TSMP was found to generally underestimate the convective area fraction, high reflectivities, and the width/magnitude of so-called differential reflectivity (Z_{DR}) columns indicative of updrafts, all leading to an underestimation of the frequency distribution for high precipitation values. The statistical distributions of Z_{DR} and specific differential phase (K_{DP}) were however similar, while the cross-correlation coefficient (ρ_{hv}) was poorly simulated, probably due to little variability of assumed hydrometeor shapes and orientations in the forward operator. The observed model bias in the Z_{DR} columns could be associated with small size of supercooled raindrops and poorly resolved three dimensional flow at km-scale simulations, besides the treatment of freezing process in the model, which warrants further research.

1 Introduction

Clouds and precipitation are the major source of uncertainty in numerical predictions of weather and climate. Especially, the parameterization of cloud microphysical processes and its interaction with the resolved dynamics need to be well tuned in order to provide dependable predictions (Igel et al., 2015; Brown et al., 2016; Morrison et al., 2020). In numerical models, the cloud microphysics is parameterized either using the so-called spectral (bin) approach or single/multi-moment bulk formulations, with the latter most common in numerical weather prediction (NWP) models due to computational efficiency (Khain et al., 2000). These parameterizations are often constrained using in-situ and/or radar reflectivity ($Z_H[dBZ]$) observations. While in-situ measurements e.g. by aircrafts are sparse, ground-based radar observations provide three-dimensional structure of microphysical processes and are thus widely used in numerical modeling evaluation (e.g., Noppel et al. 2010; Min et al. 2015; Tao et al. 2016; of many others). Polarimetric radar observations provide besides Z_H, estimates of differential reflectivity ($Z_{DR}[dB]$), specific differential phase ($K_{DP}[degkm^{-1}]$), and cross-correlation coefficient ($\rho_{hv}[-]$), which depend on hydrometeor shape, orientation, density and phase composition, and thus enable a more detailed evaluation of the modeled microphysical and macrophysical processes (Andrić et al., 2013; Snyder et al., 2017a; Putnam et al., 2017).

https://doi.org/10.5194/acp-2021-404
Preprint. Discussion started: 15 June 2021


Atmospheric Chemistry and Physics Discussions

Measured polarimetric variables are the result of the average scattering characteristics of the ensemble of hydrometeors contained in a resolved radar resolution volume, and are expressed as second order moments or correlations and powers of the horizontally and vertically polarized signals (Ryzhkov and Zrnic, 2019). Polarimetric variables are affected by hydrometeor shape/size distribution, concentration, orientation and phase composition, but all to a different extent and therefore the multivariate fingerprints provides insights into various microphysical processes like size sorting, evaporation, aggregation, riming, melting, secondary ice production etc. Horizontal reflectivity (Z_H) especially provides information on the size and with that on ongoing aggregation/riming processes. Differential reflectivity (Z_{DR}) mainly provides information on the shape of hydrometeors and does not depend on the number concentration, while specific differential phase (K_{DP}) is proportional to the concentration of hydrometeors and thus e.g. provides insights on new snow generation in the dendritic growth layer (Trömel et al., 2019). Cross-correlation coefficient (ρ_{HV}) is mainly a measure for the diversity of hydrometeors in the resolved radar resolution bin. These informations can be used for numerical model evaluation using two approaches: (1) the comparison of simulated mixing ratios or process rates with microphysical and thermodynamic retrievals from radar observations and (2) the direct comparison in radar observation space exploiting synthetic measurements obtained from a forward operator (Ryzhkov et al., 2020; Trömel et al., 2021). While both approaches have uncertainties caused by inherent assumptions, the latter method recently received more attention in the community due to increasingly available forward operators (e.g. Xie et al. 2016; Oue et al. 2020), but requires awareness of assumptions made in both the model and the forward operator.

The Terrestrial Systems Modeling Platform (TSMP: Shrestha et al. 2014; Gasper et al. 2014) was developed to better represent biogeophysical processes in regional coupled atmosphere-landsurface models with explicit representation of surface groundwater interactions and to eventually improve modeled land-atmosphere interactions and system state predictions (Simmer et al., 2015). TSMP has been extensively evaluated over north-western Germany for hydrological processes and land-atmosphere interactions (Shrestha et al., 2014; Rahman et al., 2015; Sulis et al., 2015; Uebel et al., 2017; Shrestha, 2021a): So far, however, polarimetric radar observations, which offer in-depth information on clouds and precipitation microphysical composition and evolution, have not yet been exploited for the evaluation of the modeling platform.

Evaluation of model in radar space has its own challenges due to uncertainties in assumptions made e.g. about scattering properties of hydrometeors, melting parameterizations, effective medium approximation (EMA) etc. in the forward operator and due to uncertainties associated with polarimetric measurements from radar data. The polarimetric variables Z_H and Z_{DR} are e.g. affected by radar miscalibration, partial beam blockage and (differential) attenuation, especially at smaller wavelengths (C band and X band), and their correction especially in deep convective, hail-bearing cells gives rise to additional uncertainties(e.g. Snyder et al. 2010). In contrast, K_{DP} is not affected by miscalibration and attenuation affects, but significant components of backscatter differential phase (δ) in total differential phase shift (Φ_{DP}—when hydrometeor sizes are in the range of or larger than the radar wavelength) complicate reliable estimation. These so-called resonance effects are most pronounced at C band but also significant at X band (Trömel et al., 2013).

Many previous studies have documented polarimetric signatures of convective storms in S band or C band observations (e.g., Kumjian and Ryzhkov 2008, 2012; Homeyer and Kumjian 2015; Kaltenboeck and Ryzhkov 2013), while studies based on high-resolution X band observations is still gaining grounds (e.g., Kim et al. 2012; Snyder et al. 2010, 2013, 2017a; Figueras i

https://doi.org/10.5194/acp-2021-404
Preprint. Discussion started: 15 June 2021


Atmospheric Chemistry and Physics Discussions

Ventura et al. 2013; Suzuki et al. 2017). Therefore, the main goal of this study is to use ensemble TSMP simulations in conjunction with forward operator to evaluate the simulated cloud microphysical processes in radar space for multiple summertime convective storms over north-western Germany using attenuation corrected observations from the X-band radars.

The rest of the manuscript is structured as follows: Section 2 describes the TSMP model and polarimetric radar observation operator. The experimental setup including the observations used to evaluate the model are discussed in Sect. 3. The synoptic conditions for the simulated cases are described in Sect. 4. Results of model evaluation in radar space, including the comparison with radar based precipitation estimates and stream flow measurements are presented in Sect. 5. Discussion and conclusions are provided in Sect. 6 and 7 respectively.

2 Model and Forward Operator

2.1 Model

The Terrestrial Systems Modeling Platform (TerrSysMP or TSMP; Shrestha et al. 2014; Gasper et al. 2014; Shrestha and Simmer 2020) connects three models for the soil-vegetation-atmosphere continuum using the external coupler OASIS3-MCT (Craig et al., 2017). The soil-vegetation component consists of the NCAR community Land Model CLM3.5 (Oleson et al., 2008) and the 3D variably saturated groundwater and surface water flow model ParFlow (Jones and Woodward, 2001; Ashby and Falgout, 1996; Kollet and Maxwell, 2006; Maxwell, 2013). The atmospheric component consists of the operational German weather forecast model COSMO (Consortium of Small-scale Modelling; Doms and Schättler 2002; Steppeler et al. 2003; Baldauf et al. 2011). COSMO uses the Runge-Kutta dynamical core to solve the compressible Euler equations using the modified time-splitting approach of Wicker and Skamarock (2002). The equations are formulated in a terrain-following coordinate system with variable discretization using the Arakawa C-grid. The physical packages used in this study are the radiation scheme based on the one-dimensional two-stream-approximation of the radiative transfer equation (Ritter and Geleyn, 1992), a shallow convection scheme based on (Tiedtke, 1989), a 2-moment bulk microphysics scheme (Seifert and Beheng 2006, hereafter referred as SB2M) and a modified turbulence level 2.5 scheme of Mellor and Yamada (1982)(Raschendorfer, 2001). We discuss the cloud microphysics scheme relevant for this study in more detail below; more detailed discussions of the dynamical and physical processes in COSMO can be found in Baldauf et al. (2011).

SB2M is used in an extended version with a separate hail class (Blahak, 2008) and a new cloud droplet nucleation scheme based on lookup tables (Segal and Khain, 2006) and raindrop size distributions with the shape parameter dependent on the mean diameter for sedimentation and evaporation (Seifert, 2008; Noppel et al., 2010). SB2M predicts the water mixing ratios (q_x) and number densities (N_x) of cloud droplets, rain, cloud ice, snow, graupel and hail particles, which are all assumed to follow a generalized Gamma distribution,

$$f(x) = N_o x^{\nu} exp(-\lambda x^{\mu}) \tag{1}$$

where x is the mass of the hydrometeor and N_o, μ, ν and λ are the intercept, spectral shape and slope parameters, respectively. While the shape parameters are prescribed, N_o and λ can be estimated using the zeroth and the first moments of the distribution.

https://doi.org/10.5194/acp-2021-404
Preprint. Discussion started: 15 June 2021


Atmospheric Chemistry and Physics Discussions

The equivalent/maximum diameter (D_x) of spherical/non-spherical hydrometeors is given by

$$D_x = ax^b \tag{2}$$

The shape parameters of the Gamma distribution (Eq. 1) and and power law relationship between diameter and particle mass (Eq. 2) for different hydrometeors used in this study are summarized in Table 1. Further, SB2M does not have a prognostic melted fraction, and instantaneously transfers the amount of meltwater formed during one model timestep from cloud ice, snow, graupel, and hail to the rain class.

The background aerosol physical and chemical properties are parameterized in the SB2M via condensation nuclei (CN) concentration (N_{cn}, m^{-3}), mean radius of the dominant mode of the aerosol size distribution $(R_2, \mu m)$, the logarithm of its geometric standard deviation $log(\sigma_s)$, and solubility (ϵ_s). The number density for ice nuclei $(IN; N_{x=dust,soot,organics}, m^{-3})$ is prescribed for heterogeneous ice nucleation based on the parameterization of Kärcher and Lohmann (2002) and Kärcher et al. (2006). The vertical profile of the CN concentration is assumed constant up to 2 km height followed by an exponential decay above. Table 2 summarizes the large-scale aerosol specification for the cloud droplet and ice particle nucleation used in this study. In absence of an prognostic aerosol model, the prescribed values remain constant, and processes like scavenging or chemical transport are not modeled.

2.2 Forward Operator

The Bonn Polarimetric Radar forward Operator (B-PRO;Xie et al. 2021) used in this study is a polarimetric extension of the non-polarimetric EMVORADO (Zeng et al., 2016) operator, which computes the polarimetric radar variables from scattering amplitude calculations using the T-matrix method (Mishchenko et al., 2000). The synthetic polarimetric moments are ouput on the spatial grid given by the numerical model field.

B-PRO simulates the polarimetric radar variables at specified weather radar wavelengths (e.g., X-band—3.2 cm) using prognostic model states of temperature, pressure, humidity, wind velocity, mixing ratio and number densities of hydrometeors. Besides cloud liquid class, the hydrometeors are interpreted as homogeneous oblate spheroids in the T-matrix computation. Additional uncertainties in the polarimetric estimates arise from required hydrometeor information usually not available from the model like spheroid diameter (D_x), aspect ratio (AR), width of canting angle distributions σ_c, and dielectric constant. The latter is further dependent on hydrometeor density, water content, temperature and liquid-ice phase partitioning, and a selection of effective medium approximation available for ice-air and water-ice-air mixtures. Since SB2M does not have a prognostic melted fraction, B-PRO uses melting parameterization for treatment of melting hydrometeors. Table 3 summarizes the parameters used to estimate the scattering properties of the modeled hydrometeors in the forward operator. The diameter size distribution $f(D_x)$ is calculated for all hydrometeors based on the estimated parameters of the Gamma distribution N_o and λ (Eq. 1) using the shape parameter (Table 1) and model outputs of q_x and N_x. For rain below clouds $(q_c = 0)$, the shape parameter is diagnosed from of q_r and N_r, using the $\mu - D_m$ relationship for rain (Seifert, 2008). More details about the B-PRO is also available from (Shrestha et al., 2021).

https://doi.org/10.5194/acp-2021-404
Preprint. Discussion started: 15 June 2021


Atmospheric Chemistry and Physics Discussions

Since T-matrix computations are computationally very expensive in the absence of look-up tables, B-PRO simulations are performed only for a cropped model domain (180x180x80 grid points) and for limited time periods. We also decomposed the model grid area into smaller sub-domains (20x20x80 grid points), such that B-PRO can be run in parallel for those in order to further speed-up the T-matrix computations.

3 Experiment Setup

3.1 Model Domain

The experiment is setup over the Bonn Radar domain (Shrestha, 2021a) - a temperate region in the northwestern part of Germany bordering with the Netherlands, Luxemburg, Belgium, and France (Fig. 1a). The region has a quite heterogeneous land cover and comprises extensive emissions by point (e.g., oil refineries, photochemical industries) and area sources (e.g., extensive urban and rural areas, road transport, extensive agriculture, railways) (Kulmala et al., 2011; Kuenen et al., 2014). The twin polarimetric X-Band research radars in Bonn (BoxPol) and Jülich (JuxPol) and the overlapping measurements from four polarimetric C-Band radars of the German Weather Service (Deutscher Wetterdienst, DWD) make the region probably the best radar-monitored area in Germany. The model domain covers approximately 333x333 km^2 area with a horizontal grid resolution of 1.132 km. Eighty level are used in the vertical with a near-surface-layer depth of 20 m for the atmospheric model. For the hydrological model, 30 vertical levels with 10 stretched layers in the root zone (2–100 cm) and 20 constant levels (135 cm) below is used, extending down to 30 m below the surface.

The land cover type and associated phenology is based on the Moderate Resolution Imaging Spectroradiometer (MODIS) remote sensing products (Friedl et al., 2010; Myneni et al., 2015). The Rhein massif intersected by the Middle Rhein valley dominates its topography, and forested areas (58%), agricultural land (23%), urban areas (12%) and grasslands (7%) characterize the land-cover. The root zone soil texture is mostly dominated by loamy soil with patches of sand, sandy-loam and clay-loam. The soil texture pattern below the root zone matches well with the topography—with valleys dominated by highly productive porous aquifers and practically non-aquiferous rocks over the hills.

3.2 Simulations

Ensemble simulations for three case studies comprising in total 60 model runs are used to quantify the uncertainty in the simulated precipitation and polarimetric variables. The 20 ensemble members of the COSMO-DE Ensemble Prediction System (EPS; Gebhardt et al. 2011; Peralta et al. 2012) representing uncertainties in model physics and lateral boundary conditions by combining five model physics perturbations with four global models are used for the initial and lateral boundary condition (IC/BC) of the atmospheric states, which dominate uncertainty for longer lead times. The general statistics of the EPS are always stratified according to four global models when used for IC/BC perturbations of COSMO-DE; i.e. the five members having the same global model are more similar to each other (personal communication: G. Christoph, DWD). Since January 2015, the ICON (ICOsahedral Non-hydrostatic, Zängl et al. 2015) modeling framework was used instead of the global numerical

https://doi.org/10.5194/acp-2021-404
Preprint. Discussion started: 15 June 2021


Atmospheric Chemistry and Physics Discussions

weather prediction model GME (Majewski et al., 2002). Also, the EPS system was switched to BCs based on ICON-EU-EPS and IC perturbations generated by a Local Ensemble Kalman Filter from March 2017 onwards.

The initial soil-vegetation states are obtained from spinups using offline hydrological model runs over the same domain (Shrestha, 2021b). In all runs, a coupling frequency of 90 s is used between the atmospheric and hydrological components, which have a time steps of 10 s and 90 s, respectively. The models are integrated over diurnal scale starting at mid-night. The atmospheric model output is generated at 5 min intervals, while the hydrological model output is generated at hourly intervals. For the third case, the internal variability in the ensemble members was relatively high in terms of the spatio-temporal distribution of convective storms (probably associated with the switching of the ensemble generator in 2017); thus the output was generated at 15 min intervals over a longer model period in order to allow for a fair comparison with observations and to maintain the same load for synthetic polarimetric processing and data storage.

The ensemble simulation per event required an average of 54 core-hours using 456 compute cores on the JUWELS machine at Jülich Supercomputing Center (JSC). Approximately 540 GB of data were produced per event. For polarimetric variables, only 3 hourly data containing 37 time snapshots were processed for each simulation on a local linux cluster (CLUMA2), amounting to 220 GB per event.

3.3 Observations

The observed polarimetric radar variables used in this study are based on the twin research X-band Doppler radars located in Bonn and Jülich (BoxPol and JuXPol; Diederich et al. 2015a, b), which operate at a frequency of 9.3 GHz with a radial resolution of 100-150 m and a scan period of 5 minutes. Z_H was calibrated by comparison with observations of the Dual-frequency Precipitation Radar (DPR) onboard the Global Precipitation Mission (GPM) Core Observatory satellite. To this goal, both observations are first brought to the same observational volumes, then the melting layer is identified and excluded from the calculation of the median. The DPR serves as the reference, as it is assumed to be well calibrated (Pejcic et al., 2021).

The Z_{DR} calibration uses vertical scans where near-zero Z_{DR} are expected. Values with $\rho_{hv} < 0.9$ are filtered out to avoid impacts of non-meteorological scatterers, and $Z_H > 30\ dBZ$ are ignored to keep only stratiform events. The melting layer and the near-radar gates (first 600m) are also removed to reduce noise and the offset calculated as the median of the remaining values (Williams et al., 2013; Ryzhkov and Zrnic, 2019). Futher adjustments are made for both Z_H and Z_{DR} based on a comparison between BoXPol and JuXPol. The radar calibration varies with time; see table in A1 for observed offsets for the different events.

Corrections for attenuation and differential attenuation especially due to hail follows the algorithm from Ryzhkov et al. (2013). The algorithm first identifies radial segments with potential hail along the beam via ($Z_H > 50\ dBZ$). For these segments, the coefficient for attenuation is calculated via the ZPHI method from Testud et al. (2000). Differential attenuation due to the presence of hail is calculated by comparing the observed Z_{DR} behind the hotspot with an expected value based on Z_H (at values between 20 and 30 dBZ to ensure light rain, Eq. 11 in Ryzhkov et al. (2013)) and use the difference to calculate the value of the differential attenuation coefficient in the hail core. For other segments, the standard linear relationships between attenuation and differential attenuation and differential phase (ϕ_{DP}) are used with standard coefficients for X band from (Ryzhkov

https://doi.org/10.5194/acp-2021-404
Preprint. Discussion started: 15 June 2021


Atmospheric Chemistry and Physics Discussions

and Zrnic, 2019) ($\alpha = 0.28$ and $\beta = 0.03$). These coefficients are not used for the hail inflicted segments for which we do not know the actual attenuation and differential attenuation—the above method only provides estimates of attenuation-corrected Z_H and Z_{DR}. We acknowledge this uncertainty in the estimates of attenuation corrected radar observations.

We also further interpolated the polarimetric radar data from the native polar coordinates to cartesian coordinates at 500 m horizontal and vertical resolution using a Cressman analysis with a radius of influence of 2 km in the horizontal and 1 km in the vertical. While, the data in native polar co-ordinates is used for investigating polarimetric signatures, the gridded data allows for easy comparisions with their model-simulated equivalents. Ground clutter and non-meteorological scatterers are known for having significantly decreased values of ρ_{hv} compared to precipitation (Zrnic and Ryzhkov, 1999; Schuur et al., 2003). A threshold of 0.8 in ρ_{hv} was imposed in the gridded data to ensure that clutter is filtered out without removing useful meteorological information.

Besides, the observations from the X-band radars, the RADOLAN (Radar Online Adjustment; Ramsauer et al. (2018),Krklow et al. (2020)) data from the German national meteorological service (DWD, Deutscher Wetterdienst) is also used for evaluating the modeled precipitation. RADOLAN is a gauge adjusted precipitation product based on DWD's C-band weather radars available at hourly frequency in a spatial resolution of 1 km. Finally, streamflow observed by 104 stations within the model domain from the Global Runoff Data Center, 56068 Koblenz, Germany (GRDC) is used for evaluating the modeled discharge. Station observations are mapped into the model grid when available for the events and when the respective catchment area is represented in the model within $\pm 20\%$ using the TSMP Pre-processing and Post-processing System (TPS; Shrestha 2019), which resulted in 36 useful stations.

4 Case Studies

4.1 Synoptic situations

The first case (5 July 2015) is a northeastward propagating deep convective hail-bearing storm crossing Bonn. The storm was connected to low-pressure system west of Ireland with an occluded front crossing Norway and the cold front extending over the western part of middle Europe producing pre-frontal convergence zones over western Germany, where a moisture tongue ahead of the cold front produced instability and drew warm moist air mass from the south. Scattered notheasterly propagating storms were prevalent throughout the day, with an isolated deep convective storm passing directly over the Bonn radar from 1500 to 1600 UTC. Acccording to the European Severe Weather Database (ESWD), large hail (2 - 5 cm in diameter) was observed over the Bonn region, including damaging lightnings further north, and heavy precipitation with severe wind (further north-east).

The second case (13 May 2016) is chracterized by scattered convective storms over Rheinland Pfalz, Germany, connected with a low pressure system over the Norwegian sea with an occluded front over northern and a cold front over southern Germany. The southward propagating cold front provided the necessary lift to release the potential instability associated with a warm moist air mass below 700 hPa over the region between the occlusion and the cold front. The ESWD reported heavy rainfall over the Frankfurt area resulting in flooding and damage to property.

https://doi.org/10.5194/acp-2021-404
Preprint. Discussion started: 15 June 2021


Atmospheric Chemistry and Physics Discussions

The third case (6 July 2017) consists of deep convective clouds propagating eastwards over Bonn. On that day, a warm front over middle of Germany separated a relatively cool northern, from a warm southern Germany. A low pressure system over the North Atlantic produced an occlusion west of UK moving eastward, which pushed the western edge of the warm front—disturbing it into a wave like feature. The induced anticlockwise rotation of the warm front produced the necessary lift to release the potential instability associated with the warm and moist southerly air mass. The ESWD reported scattered severe wind around the Bonn region and heavy precipitation south of Mainz including large hail.

5 Results

5.1 Accumulated Precipitation

First, we examine the model simulated ensemble precipitation with the RADOLAN data. Overall, the spatial pattern of ensemble averaged accumulated precipitation resemble the RADOLAN estimates, but the frequency distribution produced by the ensemble members underestimate high precipitation for all three cases leading to a weak precipitation gradient in the ensemble average. For the first case (Fig. 2 a), the model simulated accumulated precipitation is stratified according to four global models used for IC/BC. The members using GME data produce average accumulated precipitation and a frequency distribution for average accumulated precipitation (< 30 mm) closest to RADOLAN. The model does, however, underestimate average accumulated precipitation (> 30 mm) for all ensemble members as also visible in the spatial pattern of the ensemble averaged accumulated precipitation. While the large-scale extent of the precipitating area is comparable between model and RADOLAN, the precipitation amount especially in the northwestern domain is underestimated. For the second case (Figure 2b), all ensemble members underestimate the average accumulated precipitation compared to RADOLAN; also its frequency distribution for high precipitation is weaker compared to the first case. All ensemble members for second case, underestimates average accumulated precipitation (> 10 mm). For the third case (Fig. 2 c), the model misses the precipitation observed over the western part of the domain for all ensemble members except of one, and the simulated frequency distribution of accumulated precipitation exhibits a larger spread. This could be attributed to the switch in the ensemble generator for large scale atmospheric forcing data.

5.2 River discharge

Overall, the model generally does not produce sufficient base flow compared to the GRDC observations (Figure 3), which we mainly attribute to the still coarse grid resolution compared to actual river widths (Schalge et al., 2019). The model does, however, produce reasonable daily mean discharge compared to GRDC data for rivers with catchment areas covered by the storm's precipitation. The spatial pattern and intensity of simulated precipitation as such exhibits strong controls on the simulated discharge. In the first case study, the model ensemble exhibits a spread in the simulated discharge with varying precipitation amounts for Lippe river (two different locations) in North-Rhine Westphalia and Ems river in the north-western Germany.

https://doi.org/10.5194/acp-2021-404
Preprint. Discussion started: 15 June 2021


Atmospheric Chemistry and Physics Discussions

Similarly, the model ensemble also exhibits a spread in the simulated discharge for Nettebach in North-Rhine Westphalia and Wied river in Rhineland-Palatinate for the second case.

5.3 Polarimetric Signatures

For a given precipitation type, polarimetric variables are expected to cluster in a specific region of the multi-dimensional space (Zrnic and Ryzhkov, 1999). Thus as one evaluation method, we compare the respective clustering between simulations and observations for similar stages of convection, which we identify via the Convective Area Fraction (CAF, area fraction of a storm with radar reflectivity >40 dBZ at 2 km height a.g.l; Fig. 4) and by a qualitative exploratory analysis of the model ensembles and the observed storm evolution. For the first case, the observed storm CAF decreases while approaching the radar and increases again while moving away from the radar. Especially, the ensemble members initiated and forced with GME model (relatively dark lines) show a similar behaviour but underestimate CAF compared to observations. For the second case, CAF gradually increases for all ensemble members as in the observations, but CAF is underestimated in the earlier storm phase (before 1100 UTC). For the third case, the simulated CAFs of the model ensembles have a wider spread, probably caused by a switch in the way the ensemble is generated from March 2017 onwards. While few ensemble members simulate the storm much earlier than observed (relatively dark lines), the CAF of one ensemble member, better matches the observations and exhibits also a storm evolution (dark line) quite similar to the observations.

Based on the CAF time-series and qualitative exploratory analysis of storm evolution, we identified optimal locations (identified by square markers) and time intervals (solid lines bounded by vertical bars) for the comparison of the statistical distribution of polarimetric variables between observations and simulations.

Importantly, both synthetic and observed radar variables are affected by errors in forward operator and calibration/attenuation corrections respectively. The errors in the forward operator could mainly arise due to many assumptions that need to be made regarding the hydrometeor scattering properties, melting parameterizations, effective medium approximations (EMA) etc. Similarly, errors in observed radar data might arise due to the assumptions made in the attenuation correction algorithm. We acknowledge this limitation in the study, and concentrate more on patterns and not so much on the actual magnitudes of the polarimetric moments.

5.3.1 Case One

Fig. 5 a shows the Plan Position Indicator (PPI) plots of Z_H, Z_{DR}, K_{DP} and ρ_{hv} at 8.2 degree elevation observed by BoXPol at 1530 UTC for the first case. The storm is characterized by high reflectivity (>50 dBZ) and differential reflectivity (> 2 dB) near the melting layer. An arc-like feature of high Z_{DR} follows the leading eastern edge of the storm just below the melting layer with concurrent lower Z_H values suggesting hydrometeor size sorting associated with storm inflow (Kumjian and Ryzhkov, 2012; Dawson et al., 2014; Suzuki et al., 2017). Fig. 5 b shows a cross-section of storm based on the gridded radar data. Its convective part between -20 and 5 km relative to BoXPol exhibits Z_{DR} columns, anchored to lower levels and extending up to 6 km altitude associated with two strong updraft zones. Their different extensions suggest different updraft intensities including frozen drops aloft (Kumjian and Ryzhkov, 2008; Kumjian et al., 2014; Snyder et al., 2015). K_{DP} columns (Ryzhkov

https://doi.org/10.5194/acp-2021-404
Preprint. Discussion started: 15 June 2021


Atmospheric Chemistry and Physics Discussions

and Zrnic, 2019; Snyder et al., 2017b) co-located with the Z_{DR} columns with slight inward offsets are additional signs for updraft locations (e.g., van Lier-Walqui et al. 2016). The low (<0.7) cross-correlation coefficient (ρ_{hv}) near the inflow region and the still low ρ_{hv} (<0.92) along the strong convective core associated with high reflectivity probably indicates hail. The dominance of near-zero Z_{DR} and reflectivity values between 20 and 25 dBZ above the melting layer in the anvil suggest the dominance of snow (Yuter and Houze Jr, 1995). The low ρ_{hv} in the northern region at higher levels associated with relatively high Z_{DR} and moderate K_{DP}, are probably caused by horizontally oriented ice crystals.

As discussed in Sect. 5.1, the ensemble members initiated using GME data have similar storm evolutions as observed. So, only these ensemble members are used here for the polarimetric comparisons. Fig. 6 shows the simulated polarimetric moments at lower levels up to the melting layer and cross-sections of polarimetric variables and simulated hydrometeors at 1455 UTC for one of the ensemble members (Fig. 4 a—dark solid line). At lower levels (1000 m a.g.l.), the southeastern flank of the storm has - as expected near the core of the storm - relatively high Z_H and Z_{DR} (also associated with relatively low ρ_{hv}) with lower magnitudes on the northwestern side. K_{DP} has generally low magnitudes while ρ_{hv} is generally high. Near the melting level (4000 m a.g.l.), K_{DP} present much lower magnitudes but ring like feature of Z_{DR} with relatively low ρ_{hv} is visible in the updraft region, which is a typical polarimetric signature found for supercell storm (Kumjian and Ryzhkov, 2008).

In all ensemble members, the storm is aligned in the northeast direction and has a strong updraft region in the southeasten edge characterized by a bounded weak echo region (BWER, see Fig. 6 c). The convective storm top extends up to 15 km height with Z_H between 30 and 40 dBZ (which is relatively lower than the observed Z_H) co-located with the simulated hail shaft and updraft (Fig. 6 d). The model also exhibits a narrow Z_{DR} column extending up to 6 km altitude adjacent to the updraft region. The simulated Z_{DR} column is relatively smaller in width and magnitude (value) compared to the observations. The model also simulates high K_{DP}(> 1 deg/km) along the top of the convective storm part, but no K_{DP} columns are present in the updraft region as seen in the observations. Although, the simulated ρ_{hv} is higher than observed, slight decrease can be observed in the updraft region with high Z_H associated with hail, and below the melting layer.

In the updraft region, the modelled vertical velocity above 8 km reaches 40 m/s, dominated mostly by super-cooled raindrops around 6-9 km (see Fig. 6 d), which is an important source for hail growth. The strong updraft also generates a warm anomaly above the melting layer (see the 0° isotherm), below which rain is also formed by melting of graupel and hail. Graupel dominates the frozen hydrometeor categories above the melting layer peaking at top of the updraft region. Ice crystals are located mostly above 8 km height, and the self-collection of these ice particles leads to the formation of snow which further grows in size via aggregation. Low concentration of hails are also simulated on periphery of the peak updraft.

5.3.2 Case Two

Fig. 7 shows the PPIs of Z_H, Z_{DR}, K_{DP} and ρ_{hv} at 1.0 degree elevation from BoXPol at 1030 UTC for the second case. We find moderate reflectivities (35 - 40 dBZ) and high Z_{DR} (>2 dB) at around 1 km. According to the cross-section of storm based on gridded polarimetric radar data (Fig. 7 b), the storm has a wide Z_{DR} column anchored to the lower levels and extending up to 5 km. At this location, below the melting layer (approx. 2.5 km), Z_{DR} is >2 dB while reflectivity is weak, which suggests size-sorting of rain drops. A large portion of the storm exhibits very low or negative Z_{DR} above the melting layer, possibly

https://doi.org/10.5194/acp-2021-404
Preprint. Discussion started: 15 June 2021


Atmospheric Chemistry and Physics Discussions

indicating vertically oriented or conical graupel (Bringi et al., 2017). While other studies also have shown the presence of low and negative Z_{DR} above melting layer for convective storms (e.g Suzuki et al. 2017; Hubbert et al. 2018), it is possible that for these convective cases, attenuation correction even with the advanced methods as we used here may at least partially contribute to negative Z_{DR}.

Figure 8a,b shows the simulated polarimetric moments up to near the melting layer and cross-sections of polarimetric variables and simulated hydrometeors at 1050 UTC for one of the ensemble members (see Fig. 4 b—thick solid line). The southwards propagating storm is oriented in north-south direction. Regions with moderate to high reflectivities in the lower levels (1000 m a.g.l.) coincide with moderate to high Z_{DR}, K_{DP} and lower ρ_{hv} suggesting heavy rain or rain/hail mixtures. Just above the melting level (3000 km a.g.l.), Z_{DR} and K_{DP} are much lower except on the western storm edges, where Z_{DR} and K_{DP} columns are found (but with weak magnitudes). According to the cross-section (Fig. 8 c) moderate reflectivities (30-50 dBZ) comparable to the observations, reach up to 6 km height while the storm top height extends up to 9 km. Narrow Z_{DR} columns with lower ρ_{hv} extend up to 7 km and signal high rain concentration and hail above the melting layer (Fig. 8d). Again, the simulated Z_{DR} column is much smaller in width and magnitude compared to the observations. A grid-scale K_{DP} extended upto 4 km above the melting layer is also visible but K_{DP} generally, remains very low here except for some region near the storm top, which is also visible in the observations.

Based on the modeled hydrometeors, Fig. 8 d indicates presence of super-cooled raindrops above the melting layer connected with updraft regions (5 m/s maximum vertical velocity at the left and right edges of the storm). However, the smaller size of raindrops (< 1 mm) are not sufficient to create strong Z_{DR} magnitudes as observed in the Z_{DR} columns. The vertical velocity in the storm center is around 1 m/s and not included in the contour plot. The frozen hydrometeors are again dominated by graupel with high concentrations in the strong updraft region. Some hail is present adjacent to the updraft regions reaching down to the surface. Above 6 km height some cloud ice exists while this region is mostly dominated by snow.

5.3.3 Case Three

Fig. 9 shows the PPIs of Z_H, Z_{DR}, K_{DP} and ρ_{hv} at 8.2 degree elevation from BoXPol at 1400 UTC. The storm is characterized by reflectivities > 50 dBZ and Z_{DR} >2 dB near the melting layer. Its convective region (reflectivities ´> 50 dBZ) extends up to 12 km height and the correspoding lower ρ_{hv} indicate presence of hail (Figure 7b). The convective core has also relatively high K_{DP} values extending up to the storm top and including a wide Z_{DR} column up to 5 km height. Both indicate lofting and growth of large rain drops by updrafts, which are also important for hail formation. This case also shows low to negative Z_{DR} values above the melting layer, which could also be partially contributed by the attenuation correction algorithm.

Fig. 10 shows the polarimetric variables up to the melting layer and a cross-sections of them including hydrometeors at 1530 UTC simulated by one of the ensemble members (see Fig. 4 c—thick solid line). The eastward propagating storm is oriented from west to east and at lower levels characterized by a wide core of moderate reflectivity (40-50 dBZ) and high K_{DP}, Z_{DR} >2 dB along the edges, and low ρ_{hv} produced by heavy rain and rain/hail mixtures. Near the melting level (4000 m a.g.l.), variable Z_{DR} and Z_H regions are found near the southeastern edge—characteristics of rain drop size-sorting. Overall, Z_{DR} and K_{DP} are low throughout the storm. According to the cross-section (Fig. 10 c) the storm extends up to 12 km with

https://doi.org/10.5194/acp-2021-404
Preprint. Discussion started: 15 June 2021


Atmospheric Chemistry and Physics Discussions

moderate reflectivities (30-50 dBZ). While, Z_H at lower levels is comparable to observations, the relatively high Z_H seen in the observations extending upto upper levels is underestimated by the model. The model also simulates a narrow Z_{DR} column extending up to 5 km adjacent to the updraft region and relatively comparable to observation. This region also has relatively high Z_{DR} than the background, extending upto 12 km height. The model also simulates high K_{DP} along this convective part of the storm. The simulated ρ_{hv} is again generally high with slight decrease in the updraft region and below the melting layer. Similar features of Z_{DR}, K_{DP} and ρ_{hv} is also seen in the observed convective core.

The vertical velocity reaches to 10 m/s from 6-11 km in the updraft region where a low concentration of super-cooled rain drops is found up to 8 km (Fig. 10 d). Graupel again dominates the frozen hydrometeor categories above the melting layer, while snow further extends downwards upto 6 km height. Compared to the other two cases the simulated hail concentration is higher and extends below the melting layer where it contributes to rain via melting.

5.4 Frequency distribution of polarimetric variables

Mismatches between space and time scales of simulated polarimetric moments compared to observations also needs to be addressed by monitoring ensemble properties of the convective event. So, the ensemble simulations are compared to the observations for similar storm evolution stages using contoured frequency altitude diagrams (CFADs; Yuter and Houze Jr 1995) using the same extents and bin widths for observations and simulations.

5.4.1 Case One

We use the observations from 1445 to 1530 UTC, which encompasses the convective stage of the storm before it passes over the BoXPol. The CFADs from the X-band radar (Fig. 11 a) show a unimodal distribution of Z_H which gradually narrows above the melting layer (around 4 km). The peak in the frequency distribution occurs around 20-25 dBZ with maximum reflectivities well above 50 dBZ. The Z_{DR} also exhibits a narrow unimodal distribution which further peaks (or narrows) above the melting layer with the mode around 0.25 dB, similar to the values reported by (Yuter and Houze Jr, 1995) for convective storms. The distribution broadens and shifts to values up to 4 dB below the melting layer peaking at around 1 dB near the surface. K_{DP} exhibits a very narrow unimodal distribution throughout the vertical extent of storm with peak values around 0.1 deg/km. The distribution also broadens weakly from 7 km height downwards. ρ_{hv} has a quite broader distribution peaking around 0.98 below 11 km height and shifting to 0.87 near the storm top.

The CFADs from the model ensemble were generated using five members from 1445 to 1530 UTC (Fig. 4 a—soild lines) which best matched the observed storm macrophysical features. The Z_H distribution with maximum reflectivities generally below 50 dBZ peaks around 28 dBZ from 6 to 10 km, but shifts towards 15-20 dBZ at lower levels, which were found to be associated with grid cells with very low concentration of hydrometeors broadening of the distribution, compared to observations. Z_{DR} again exhibits a narrow unimodal distribution above melting layer peaking around 0.1 dB, which broadens below the melting layer with an additional peak at 2.6 dB. Unlike the unimodal CFADs from observations, the CFADs from the model ensemble produce two peaks below the melting layer. K_{DP} shows a very narrow unimodal distribution similar to

https://doi.org/10.5194/acp-2021-404
Preprint. Discussion started: 15 June 2021


Atmospheric Chemistry and Physics Discussions

the observations with peak values around 0.1 deg/km. For the given range (0.7-1.0) of ρ_{hv}, the frequency distribution appears to be poorly simulated by the model.

5.4.2 Case Two

CFADs are generated during the convective period of the storm from 1010 to 1055 UTC. The Z_H observations (Fig. 12 a) show a unimodal distribution peaking around 25 dBZ and gradually narrowing above the melting layer (3km) with maximum reflectivities > 45 dBZ. Z_{DR} also exhibits a narrow unimodal distribution peaking above the melting layer at around -0.12 dB but broadening and shifting to higher values with peaks around 0.4 dB near the surface and maxima > 2 dB below the melting layer. Compared to case one, a leftward shift can be observed for the Z_{DR} distribution, which is primarily caused by domination of low to negative Z_{DR} above the melting layer. But, similar to the first case, K_{DP} has a very narrow unimodal distribution throughout the storm with peak values around 0.1 deg/km with a very weak broadening downwards and below the melting layer. ρ_{hv} exhibits again a broader distribution peaking around 0.97 (below 7 km height) and shifting to 0.85 near the storm top.

The CFADs from the model ensemble were generated from 5 members from 1030 to 1115 UTC (see Fig. 4 b—soild lines). The CFADs for Z_H have a broader distribution compared to observation with maxima generally below 45 dBZ; the distribution peaks around 28 dBZ near the melting layer (around 3 km) and gradually shifts towards 10 dBZ near the storm top (around 8 km) and towards 32 dBZ below the melting layer. Z_{DR} has a narrow unimodal distribution above the melting layer peaking around 0.12 dB. The CFAD broadens below the melting layer with an additional peak at 2.5 dB. Again, the model CFADs produce two peaks compared to unimodal distribution for observations. Additionally, no leftward shift in the Z_{DR} distribution is observed for model ensembles as seen in observations compared to case one. K_{DP} also shows a very narrow unimodal distribution similar the observations peaking around 0.12 deg/km. The distribution weakly broadens below the melting layer and at upper levels. For the given range (0.7-1.0) of ρ_{hv}, the frequency distribution again appears to be poorly simulated by the model.

5.4.3 Case Three

CFADs are generated from 1330 to 1415 UTC. The observed unimodal Z_H distribution (Fig. 13 a) has maxima > 50dBZ and a peak around 25 dBZ which gradually narrows above the melting layer around 4km and shifts to smaller values peaking around 17 dBZ upwards above 9 km. Z_{DR} also exhibits again a narrow unimodal distribution above the melting layer with peak around -0.12 dB. The distribution broadens and shifts to larger values below the melting layer peaking around 0.4 dB near the surface with maxima > 2 dB. The Z_{DR} distribution is similar to case two. K_{DP} is very narrowly distributed throughout the storm with peak values around 0.1 deg/km but weakly broadens below the melting layer. Again, ρ_{hv} has a broad distribution peaking around 0.98 (below 8 km height) but shifting towards 0.83 at the storm top.

The CFADs from the model ensemble were generated using only 1 ensemble member from 1500 to 1545 UTC (see Fig. 4c—solid line) due to strong variability among the ensemble members. The CFADs for horizontal reflectivity have maxima below 50 dBz and again exhibit a broader distribution compared to observations, peaking around 8 and 38 dBZ near the melting

https://doi.org/10.5194/acp-2021-404
Preprint. Discussion started: 15 June 2021


Atmospheric Chemistry and Physics Discussions

layer (around 4 km) producing two peaks, and shift towards 10 dBZ near the storm top (around 10 km) and towards 42 dBZ near the surface. Z_{DR} has a narrow unimodal distribution above the melting layer with a peak around 0.1 dB and broadens below the melting layer with an additional peak at 1.5 dB. The model again produces two peaks below the melting layer and additionally do not show any leftward shift in the Z_{DR} distribution as seen between observations for case three and one. K_{DP} also shows again a very narrow unimodal distribution with peak values around 0.1 deg/km which broadens both below the melting layer and at upper levels. For ρ_{hv}, the frequency distribution again appears to be poorly simulated by the model.

6 Discussion

The variability in the lateral boundary conditions for the ensemble members was also found to generate probabilistic forecast in the accumulated precipitation, river discharges and convective area fraction (Gebhardt et al., 2011). The lateral boundary conditions affect the simulated cloud microphysical and macrophysical processes and hence both the synthetic polarimetric variables and simulated river discharges. However, the magnitude of this influence varies between the three studied cases. Particularly, the switch in the ensemble generation for the third case produced a much stronger variability in the spatiotemporal structure of the simulated storm. The CAFs from observations and model simulations indicate that the initial intensity of storms is underestimated by the model, which partly explains the underestimation of high precipitation for all ensemble members. In simulations by Noppel et al. (2010) for a hail storm over southwestern Germany using the same atmospheric model COSMO with the two moment microphysics, the continental CN concentration $(1700cm^{-3})$ led to a weaker storm and less surface precipitation compared to maritime CN concentrations $(100cm^{-3})$. However, their additional sensitivity study by varying the fixed parameters in Eq. 1 for cloud hydrometeors in order to produce a narrow distribution led to a different conclusion, indicating a missing feedback between the CN concentration and the shape parameters of the cloud droplet size distribution (which are both fixed in the model). This could also be partly contributing to the weaker initial intensity of the storms.

In general, the synthetic radar data shows that the model is able to simulate prominent polarimetric signature of the convective storms like the Z_{DR} columns, besides other additional signatures (e.g., size sorting and the ring like feature of Z_{DR} with relatively lower ρ_{hv} typically observed in supercells). Additionally, a relatively high Z_{DR} compared to the background is also visible in the updraft region for all case studies, which also appears in the observations in the convective core. While the synthetic Z_{DR} column for case three was more closer to the observed radar data, the model was found to generally underestimate the width and the magnitude (value) of the Z_{DR} column compared to observations in the remaining two cases. A reason could be the relatively small size of raindrops due to high CN concentrations. Also the missing feedback between the CN concentration and shape parameters of cloud drop size distribution (Noppel et al., 2010) and the treatment of freezing raindrops (which do require an additional hydrometeor class) could be a reason (Kumjian et al., 2014).

Below the melting layer in the downdraft regions, where the melting of graupel and hail are the main source of rain water and produce high Z_{DR}, simulations well replicate the observations. Above the melting layer, the partitioning of the ice water content in the model is generally dominated by graupel for all case studies. While case one with near zero Z_{DR} and reflectivities between 20-25 dBZ indicate domination of snow in the anvil region, low to negative Z_{DR} above the melting layer for case two

https://doi.org/10.5194/acp-2021-404
Preprint. Discussion started: 15 June 2021


Atmospheric Chemistry and Physics Discussions

and three possibly indicate domination of graupel, however we cannot be completely certain as it might be partially affected by the attenuation correction algorithm as discussed above.

CFADs of polarimetric variables used in this study provide a valuable data display for the evaluation of model microphysical processes. In general, the Z_H-CFADs from the observations exhibit narrow unimodal distributions peaking around 20-25 dBZ, but differ in maximum reflectivities (>50 dBZ for case one and three, >45 dbz for case two). Similarly, the observed CFADs for Z_{DR} also show narrow unimodal distribution above the melting layer, which gradually shift towards higher value near the surface for all three cases. While the pattern of Z_{DR} CFADs is similar for observations in all cases, the location of the peaks above the melting layer differ between case one (0.25 db) and other two cases (-0.12 dB). This difference in the peak of the observed Z_{DR} distribution could also point towards the possible difference in partitioning of ice water content above the melting layer as well as partial effect of attenuation correction algorithm. The Z_{DR} CFADs from the ensemble simulations also exhibits narrow distributions with peak values near zero above the melting layer, which does not differ among the three case studies, and also exhibits two peaks below the melting layer compared to unimodal distribution in observations. Also, the model tends to strongly underestimate the maximum reflectivities for case one but generally it exhibits a broader distribution of Z_H for all three cases compared to observation, with a peak around 30 dBZ above the melting layer. This higher reflectivity is caused by and the dominance of graupel as seen in the hydrometeor distribution. The dominance of graupel has also been reported in previous modeling studies (e.g., Tao et al. 2011; Lang et al. 2011; Shrestha 2011; Shrestha et al. 2015). Both the ensemble model runs and the observations produce similar narrow unimodal distribution for K_{DP} peaking around 0.1 deg/km while the CFADs of ρ_{hv} are poorly simulated by the model, probably due to the shortcomings in forward operator assumptions on diversity of hydrometeor shapes and orientation.

7 Conclusions

The TSMP model - in particular its atmospheric component COSMO with 2 moment microphysics scheme - was found to generally underestimate the initial intensity of storms in terms of convective area fraction, extreme reflectivities, and width/magnitude (value) of the Z_{DR} columns. These underestimations were also reflected in the frequency distribution for high precipitation and also broader distribution of reflectivities. The model was able to simulate similar statistical distribution of Z_{DR} and K_{DP} compared to the observations, while the observations also additionally exhibited shifts in the peak of the Z_{DR} above the melting layer, which was not observed in the model simulations. This shift in the observations, could be associated with differences in partitioning of ice water content above the melting layer as well as the partial effect of attenuation correction algorithm.

In general, ρ_{hv} was poorly simulated for all three cases - which warrants more work on polarimetry physics of the forward operator used in the study. The fixed CN concentrations and shape parameters of cloud drop size distribution could be also partly responsible for the overall too low storm intensities, thus regional measurements of CN concentrations, surface precipitation and polarimetric radar data observations could be used together to obtain improved shape parameters of cloud droplets. Importantly, prominent polarimetric signature of convective storms like the Z_{DR} column appears to be poorly resolved at km-

https://doi.org/10.5194/acp-2021-404
Preprint. Discussion started: 15 June 2021

Atmospheric Chemistry and Physics Discussions

scale simulations. Future model evaluations with polarimetric radar data should focus on hyper-resolution simulations to better resolve the three-dimensional motion and microphysical processes associated with multivariate polarimetric signatures as well as uncertainty estimates in the attenuation correction of polarimetric moments for convective cases.

Code and data availability. The source codes for the model and the forward operator used in this study are freely available from https://www.terrsysmp.org/ and https://git2.meteo.uni-bonn.de/git/pfo respectively with registration. The codes for radar calibration and attenuation correction will be made available from https://github.com/meteo-ubonn/miubrt. The data used for the model runs including initial conditions for the soil-vegetation states are available from Deutscher Wetterdiest (https://www.dwd.de/DE/leistungen/pamore/pamore.html) and https://doi.org/10.5880/TR32DB.40 respectively

.

Appendix A

Table A1. Estimated biases for Z_H and Z_{DR} for both radars and for each event

	BoXPol Z_H [dBZ]	JuXPol Z_H [dBZ]	BoXPol Z_{DR} [dB]	JuXPol Z_{DR} [dB]
5 July 2015	-3	-7	-1.4	-2.3
13 May 2016	-0.9	-5	-1	-1.95
6 July 2017	-0.5	-7	-0.8	-2.5

Author contributions. PS designed the study, conducted the model simulations and forward operator calculations, carried out the analysis, wrote the paper and obtained the grant for the study. ST aided in initial conceptualization of the study. RE processed the radar data (calibration and attenuation correction) for model comparison. ST, RE, CS aided with the analysis of the radar data.

Competing interests. The authors declare that they have no conflict of interest.

Acknowledgements. The research was carried out in the framework of the priority programme SPP-2115 "Polarimetric Radar Observations meet Atmospheric Modelling (PROM)" in the project ILACPR funded by the German Research Foundation (DFG, Grant SH 1326/1-1). We gratefully acknowledge the computing time (project HBN33) granted by the John von Neumann Institute for Computing (NIC) and provided on the supercomputer JUWELS at Jülich Supercomputing Centre (JSC). The pre-processing and post-processing of input data was done using the NCAR Command language (Version 6.4.0). The analysis of the radar data was done using the wradlib libraries (https://docs.wradlib.org/en/stable/index.html)

https://doi.org/10.5194/acp-2021-404
Preprint. Discussion started: 15 June 2021

Atmospheric Chemistry and Physics Discussions

References

Andrić, J., Kumjian, M. R., Zrnić, D. S., Straka, J. M., and Melnikov, V. M.: Polarimetric signatures above the melting layer in winter storms: An observational and modeling study, Journal of Applied Meteorology and Climatology, 52, 682–700, 2013.

Ashby, S. F. and Falgout, R. D.: A parallel multigrid preconditioned conjugate gradient algorithm for groundwater flow simulations, Nuclear science and engineering, 124, 145–159, 1996.

Baldauf, M., Seifert, A., Förstner, J., Majewski, D., Raschendorfer, M., and Reinhardt, T.: Operational convective-scale numerical weather prediction with the COSMO model: Description and sensitivities, Monthly Weather Review, 139, 3887–3905, 2011.

Blahak, U.: Towards a better representation of high density ice particles in a state-of-the-art two-moment bulk microphysical scheme, in: Proc. 15th Int. Conf. Clouds and Precip., Cancun, Mexico, vol. 20208, 2008.

Brandes, E. A., Zhang, G., and Vivekanandan, J.: Experiments in Rainfall Estimation with a Polarimetric Radar in a Subtropical Environment, Journal of Applied Meteorology, 41, 674 – 685, https://doi.org/10.1175/1520-0450(2002)041<0674:EIREWA>2.0.CO;2, 2002.

Bringi, V., Kennedy, P., Huang, G.-J., Kleinkort, C., Thurai, M., and Notaroš, B.: Dual-polarized radar and surface observations of a winter graupel shower with negative Z dr column, Journal of Applied Meteorology and Climatology, 56, 455–470, 2017.

Brown, B. R., Bell, M. M., and Frambach, A. J.: Validation of simulated hurricane drop size distributions using polarimetric radar, Geophysical Research Letters, 43, 910–917, 2016.

Craig, A., Valcke, S., and Coquart, L.: Development and performance of a new version of the OASIS coupler, OASIS3-MCT_3. 0, Geoscientific Model Development, 10, 3297–3308, 2017.

Dawson, D. T., Mansell, E. R., Jung, Y., Wicker, L. J., Kumjian, M. R., and Xue, M.: Low-level Z DR signatures in supercell forward flanks: The role of size sorting and melting of hail, Journal of the Atmospheric Sciences, 71, 276–299, 2014.

Diederich, M., Ryzhkov, A., Simmer, C., Zhang, P., and Trömel, S.: Use of specific attenuation for rainfall measurement at X-band radar wavelengths. Part I: Radar calibration and partial beam blockage estimation, Journal of Hydrometeorology, 16, 487–502, 2015a.

Diederich, M., Ryzhkov, A., Simmer, C., Zhang, P., and Trömel, S.: Use of specific attenuation for rainfall measurement at X-band radar wavelengths. Part II: Rainfall estimates and comparison with rain gauges, Journal of Hydrometeorology, 16, 503–516, 2015b.

Doms, G. and Schättler, U.: A description of the nonhydrostatic regional model LM, Part I: Dynamics and Numerics, Deutscher Wetterdienst, Offenbach, 2002.

Figueras i Ventura, J., Honoré, F., and Tabary, P.: X-band polarimetric weather radar observations of a hailstorm, Journal of Atmospheric and Oceanic Technology, 30, 2143–2151, 2013.

Friedl, M. A., Sulla-Menashe, D., Tan, B., Schneider, A., Ramankutty, N., Sibley, A., and Huang, X.: MODIS Collection 5 global land cover: Algorithm refinements and characterization of new datasets, Remote sensing of Environment, 114, 168–182, 2010.

Gasper, F., Görgen, K., Shrestha, P., Sulis, M., Rihani, J., Geimer, M., and Kollet, S.: Implementation and scaling of the fully coupled Terrestrial Systems Modeling Platform (TerrSysMP v1. 0) in a massively parallel supercomputing environment–a case study on JUQUEEN (IBM Blue Gene/Q), Geoscientific model development, 7, 2531–2543, 2014.

Gebhardt, C., Theis, S., Paulat, M., and Bouallègue, Z. B.: Uncertainties in COSMO-DE precipitation forecasts introduced by model perturbations and variation of lateral boundaries, Atmospheric Research, 100, 168–177, 2011.

Homeyer, C. R. and Kumjian, M. R.: Microphysical characteristics of overshooting convection from polarimetric radar observations, Journal of the Atmospheric Sciences, 72, 870–891, 2015.

https://doi.org/10.5194/acp-2021-404
Preprint. Discussion started: 15 June 2021

Atmospheric Chemistry and Physics Discussions

Hubbert, J. C., Wilson, J. W., Weckwerth, T. M., Ellis, S. M., Dixon, M., and Loew, E.: S-Pol's polarimetric data reveal detailed storm features (and insect behavior), Bulletin of the American Meteorological Society, 99, 2045–2060, 2018.

Igel, A. L., Igel, M. R., and van den Heever, S. C.: Make it a double? Sobering results from simulations using single-moment microphysics schemes, Journal of the Atmospheric Sciences, 72, 910–925, 2015.

Jones, J. E. and Woodward, C. S.: Newton–Krylov-multigrid solvers for large-scale, highly heterogeneous, variably saturated flow problems, Advances in Water Resources, 24, 763–774, 2001.

Kaltenboeck, R. and Ryzhkov, A.: Comparison of polarimetric signatures of hail at S and C bands for different hail sizes, Atmospheric Research, 123, 323–336, 2013.

Kärcher, B. and Lohmann, U.: A parameterization of cirrus cloud formation: Homogeneous freezing of supercooled aerosols, Journal of Geophysical Research: Atmospheres, 107, AAC–4, 2002.

Khain, A., Ovtchinnikov, M., Pinsky, M., Pokrovsky, A., and Krugliak, H.: Notes on the state-of-the-art numerical modeling of cloud microphysics, Atmospheric Research, 55, 159–224, 2000.

Kim, D.-S., Maki, M., Shimizu, S., and Lee, D.-I.: X-band dual-polarization radar observations of precipitation core development and structure in a multi-cellular storm over Zoshigaya, Japan, on August 5, 2008, Journal of the Meteorological Society of Japan. Ser. II, 90, 701–719, 2012.

Kollet, S. J. and Maxwell, R. M.: Integrated surface–groundwater flow modeling: A free-surface overland flow boundary condition in a parallel groundwater flow model, Advances in Water Resources, 29, 945–958, 2006.

Kreklow, J., Tetzlaff, B., Burkhard, B., and Kuhnt, G.: Radar-Based Precipitation Climatology in Germany—Developments, Uncertainties and Potentials, Atmosphere, 11, 217, 2020.

Kuenen, J., Visschedijk, A., Jozwicka, M., and Denier Van Der Gon, H.: TNO-MACC_II emission inventory; a multi-year (2003–2009) consistent high-resolution European emission inventory for air quality modelling, Atmospheric Chemistry and Physics, 14, 10 963–10 976, 2014.

Kulmala, M., Asmi, A., Lappalainen, H., Baltensperger, U., Brenguier, J.-L., Facchini, M., Hansson, H.-C., Hov, Ø., O'Dowd, C., Pöschl, U., et al.: General overview: European Integrated project on Aerosol Cloud Climate and Air Quality interactions (EUCAARI)–integrating aerosol research from nano to global scales, Atmospheric Chemistry and Physics, 11, 13 061–13 143, 2011.

Kumjian, M. R. and Ryzhkov, A. V.: Polarimetric signatures in supercell thunderstorms, Journal of applied meteorology and climatology, 47, 1940–1961, 2008.

Kumjian, M. R. and Ryzhkov, A. V.: The impact of size sorting on the polarimetric radar variables, Journal of the Atmospheric Sciences, 69, 2042–2060, 2012.

Kumjian, M. R., Khain, A. P., Benmoshe, N., Ilotoviz, E., Ryzhkov, A. V., and Phillips, V. T. J.: The Anatomy and Physics of ZDR Columns: Investigating a Polarimetric Radar Signature with a Spectral Bin Microphysical Model, Journal of Applied Meteorology and Climatology, 53, 1820 – 1843, https://doi.org/10.1175/JAMC-D-13-0354.1, 2014.

Kärcher, B., Hendricks, J., and Lohmann, U.: Physically based parameterization of cirrus cloud formation for use in global atmospheric models, Journal of Geophysical Research: Atmospheres, 111, https://doi.org/https://doi.org/10.1029/2005JD006219, 2006.

Lang, S. E., Tao, W.-K., Zeng, X., and Li, Y.: Reducing the biases in simulated radar reflectivities from a bulk microphysics scheme: Tropical convective systems, Journal of Atmospheric Sciences, 68, 2306–2320, 2011.

https://doi.org/10.5194/acp-2021-404
Preprint. Discussion started: 15 June 2021


Atmospheric Chemistry and Physics Discussions

Majewski, D., Liermann, D., Prohl, P., Ritter, B., Buchhold, M., Hanisch, T., Paul, G., Wergen, W., and Baumgardner, J.: The operational global icosahedral–hexagonal gridpoint model GME: Description and high-resolution tests, Monthly Weather Review, 130, 319–338, 2002.

Maxwell, R. M.: A terrain-following grid transform and preconditioner for parallel, large-scale, integrated hydrologic modeling, Advances in Water Resources, 53, 109–117, 2013.

Mellor, G. L. and Yamada, T.: Development of a turbulence closure model for geophysical fluid problems, Reviews of Geophysics, 20, 851–875, 1982.

Min, K.-H., Choo, S., Lee, D., and Lee, G.: Evaluation of WRF cloud microphysics schemes using radar observations, Weather and Forecasting, 30, 1571–1589, 2015.

Mishchenko, M. I., Hovenier, J. W., and Travis, L. D.: Light scattering by nonspherical particles: theory, measurements, and applications, 2000.

Morrison, H., van Lier-Walqui, M., Fridlind, A. M., Grabowski, W. W., Harrington, J. Y., Hoose, C., Korolev, A., Kumjian, M. R., Milbrandt, J. A., Pawlowska, H., et al.: Confronting the challenge of modeling cloud and precipitation microphysics, Journal of advances in modeling earth systems, 12, e2019MS001 689, 2020.

Myneni, R., Knyazikhin, Y., and Park, T.: MCD15A2H MODIS/Terra+Aqua Leaf Area Index/FPAR 8-day L4 Global 500m SIN Grid V006 [Data set], NASA EOSDIS Land Processes DAAC, https://doi.org/10.5067/MODIS/MCD15A2H.006, accessed 2019-03-09, 2015.

Noppel, H., Blahak, U., Seifert, A., and Beheng, K. D.: Simulations of a hailstorm and the impact of CCN using an advanced two-moment cloud microphysical scheme, Atmospheric Research, 96, 286–301, 2010.

Oleson, K., Niu, G.-Y., Yang, Z.-L., Lawrence, D., Thornton, P., Lawrence, P., Stöckli, R., Dickinson, R., Bonan, G., Levis, S., et al.: Improvements to the Community Land Model and their impact on the hydrological cycle, Journal of Geophysical Research: Biogeosciences, 113, 2008.

Oue, M., Tatarevic, A., Kollias, P., Wang, D., Yu, K., and Vogelmann, A. M.: The Cloud-resolving model Radar SIMulator (CR-SIM) Version 3.3: description and applications of a virtual observatory, Geoscientific Model Development, 13, 1975–1998, 2020.

Pejcic, V., Soderholm, J., Mühlbauer, K., Louf, V., and Trömel, S.: Five Years Calibrated Observations from the University of Bonn X-band Weather Radar (BoXPol), Scientific Data, to be submitted, 2021.

Peralta, C., Ben Bouallègue, Z., Theis, S., Gebhardt, C., and Buchhold, M.: Accounting for initial condition uncertainties in COSMO-DE-EPS, Journal of Geophysical Research: Atmospheres, 117, 2012.

Putnam, B. J., Xue, M., Jung, Y., Zhang, G., and Kong, F.: Simulation of polarimetric radar variables from 2013 CAPS spring experiment storm-scale ensemble forecasts and evaluation of microphysics schemes, Monthly Weather Review, 145, 49–73, 2017.

Rahman, M., Sulis, M., and Kollet, S.: The subsurface–land surface–atmosphere connection under convective conditions, Advances in water resources, 83, 240–249, 2015.

Ramsauer, T., Weiß, T., and Marzahn, P.: Comparison of the GPM IMERG final precipitation product to RADOLAN weather radar data over the topographically and climatically diverse Germany, Remote Sensing, 10, 2029, 2018.

Raschendorfer, M.: The new turbulence parameterization of LM, COSMO newsletter, 1, 89–97, 2001.

Ritter, B. and Geleyn, J.-F.: A comprehensive radiation scheme for numerical weather prediction models with potential applications in climate simulations, Monthly weather review, 120, 303–325, 1992.

Ryzhkov, A., Pinsky, M., Pokrovsky, A., and Khain, A.: Polarimetric Radar Observation Operator for a Cloud Model with Spectral Microphysics, Journal of Applied Meteorology and Climatology, 50, 873–894, https://doi.org/10.1175/2010JAMC2363.1, 2011.

https://doi.org/10.5194/acp-2021-404
Preprint. Discussion started: 15 June 2021

Atmospheric Chemistry and Physics Discussions

Ryzhkov, A. V. and Zrnic, D. S.: Radar polarimetry for weather observations, Springer, 2019.

Ryzhkov, A. V., Kumjian, M. R., Ganson, S. M., and Zhang, P.: Polarimetric radar characteristics of melting hail. Part II: Practical implications, Journal of Applied Meteorology and Climatology, 52, 2871–2886, 2013.

Ryzhkov, A. V., Snyder, J., Carlin, J. T., Khain, A., and Pinsky, M.: What polarimetric weather radars offer to cloud modelers: forward radar operators and microphysical/thermodynamic retrievals, Atmosphere, 11, 362, 2020.

Schalge, B., Haefliger, V., Kollet, S., and Simmer, C.: Improvement of surface run-off in the hydrological model ParFlow by a scale-consistent river parameterization, Hydrological processes, 33, 2006–2019, 2019.

Schuur, T., Ryzhkov, A., Heinselman, P., Zrnic, D., Burgess, D., and Scharfenberg, K.: Observations and classification of echoes with the polarimetric WSR-88D radar, Report of the National Severe Storms Laboratory, Norman, OK, 73069, 46, 2003.

Segal, Y. and Khain, A.: Dependence of droplet concentration on aerosol conditions in different cloud types: Application to droplet concentration parameterization of aerosol conditions, Journal of Geophysical Research: Atmospheres, 111, 2006.

Seifert, A.: On the parameterization of evaporation of raindrops as simulated by a one-dimensional rainshaft model, Journal of Atmospheric Sciences, 65, 3608–3619, 2008.

Seifert, A. and Beheng, K. D.: A two-moment cloud microphysics parameterization for mixed-phase clouds. Part 1: Model description, Meteorology and atmospheric physics, 92, 45–66, 2006.

Shrestha, P.: Characterization of Pre-Monsoon Aerosol and Aerosol-Cloud-Rainfall Interactions in Central Nepal, Ph.D. thesis, Duke University, 2011.

Shrestha, P.: TerrSysMP Pre-processing and Post-processing System, CRC/TR32 Database (TR32DB), https://doi.org/10.5880/TR32DB.37, last access: 9 March 2018, 2019.

Shrestha, P.: Clouds and Vegetation Modulate Shallow Groundwater Table Depth, Journal of Hydrometeorology, 22, 753 – 763, https://doi.org/10.1175/JHM-D-20-0171.1, 2021a.

Shrestha, P.: High resolution hydrological simulations over Bonn Radar Domain, https://www.tr32db.uni-koeln.de/search/view.php?dataID=1890, [Accessed 22. April 2021], 2021b.

Shrestha, P. and Simmer, C.: Modeled land atmosphere coupling response to soil moisture changes with different generations of land surface models, Water, 12, 46, 2020.

Shrestha, P., Sulis, M., Masbou, M., Kollet, S., and Simmer, C.: A scale-consistent terrestrial systems modeling platform based on COSMO, CLM, and ParFlow, Monthly weather review, 142, 3466–3483, 2014.

Shrestha, P., Dimri, A. P., Schomburg, A., and Simmer, C.: Improved understanding of an extreme rainfall event at the Himalayan foothills–a case study using COSMO, Tellus A: Dynamic Meteorology and Oceanography, 67, 26 031, 2015.

Shrestha, P., Mendrok, J., Pejcic, V., Trömel, S., Blahak, U., and Carlin, J. T.: The impact of uncertainties in model microphysics, retrievals, and forward operators on model evaluations in polarimetric radar space, Geoscientific Model Development, submitted, 2021.

Simmer, C., Thiele-Eich, I., Masbou, M., Amelung, W., Bogena, H., Crewell, S., Diekkrüger, B., Ewert, F., Hendricks Franssen, H.-J., Huisman, J. A., et al.: Monitoring and modeling the terrestrial system from pores to catchments: the transregional collaborative research center on patterns in the soil–vegetation–atmosphere system, Bulletin of the American Meteorological Society, 96, 1765–1787, 2015.

Snyder, J. C., Bluestein, H. B., Zhang, G., and Frasier, S. J.: Attenuation correction and hydrometeor classification of high-resolution, X-band, dual-polarized mobile radar measurements in severe convective storms, Journal of Atmospheric and Oceanic Technology, 27, 1979–2001, 2010.

https://doi.org/10.5194/acp-2021-404
Preprint. Discussion started: 15 June 2021

Atmospheric Chemistry and Physics Discussions

Snyder, J. C., Bluestein, H. B., Venkatesh, V., and Frasier, S. J.: Observations of polarimetric signatures in supercells by an X-band mobile Doppler radar, Monthly weather review, 141, 3–29, 2013.

Snyder, J. C., Ryzhkov, A. V., Kumjian, M. R., Khain, A. P., and Picca, J.: A ZDR Column Detection Algorithm to Examine Convective Storm Updrafts, Weather and Forecasting, 30, 1819 – 1844, https://doi.org/10.1175/WAF-D-15-0068.1, 2015.

Snyder, J. C., Bluestein, H. B., Dawson II, D. T., and Jung, Y.: Simulations of polarimetric, X-band radar signatures in supercells. Part II: Z DR columns and rings and K DP columns, Journal of Applied Meteorology and Climatology, 56, 2001–2026, 2017a.

Snyder, J. C., Bluestein, H. B., II, D. T. D., and Jung, Y.: Simulations of Polarimetric, X-Band Radar Signatures in Supercells. Part II: ZDR Columns and Rings and KDP Columns, Journal of Applied Meteorology and Climatology, 56, 2001 – 2026, https://doi.org/10.1175/JAMC-D-16-0139.1, 2017b.

Steppeler, J., Doms, G., Schättler, U., Bitzer, H., Gassmann, A., Damrath, U., and Gregoric, G.: Meso-gamma scale forecasts using the nonhydrostatic model LM, Meteorology and atmospheric Physics, 82, 75–96, 2003.

Sulis, M., Langensiepen, M., Shrestha, P., Schickling, A., Simmer, C., and Kollet, S. J.: Evaluating the influence of plant-specific physiological parameterizations on the partitioning of land surface energy fluxes, Journal of hydrometeorology, 16, 517–533, 2015.

Suzuki, S.-i., Maesaka, T., Iwanami, K., Shimizu, S., and Kieda, K.: X-band dual-polarization radar observations of the supercell storm that generated an F3 tornado on 6 May 2012 in Ibaraki Prefecture, Japan, Journal of the Meteorological Society of Japan. Ser. II, 2017.

Tao, W.-K., Shi, J. J., Chen, S. S., Lang, S., Lin, P.-L., Hong, S.-Y., Peters-Lidard, C., and Hou, A.: The impact of microphysical schemes on hurricane intensity and track, Asia-Pacific Journal of Atmospheric Sciences, 47, 1–16, 2011.

Tao, W.-K., Wu, D., Lang, S., Chern, J.-D., Peters-Lidard, C., Fridlind, A., and Matsui, T.: High-resolution NU-WRF simulations of a deep convective-precipitation system during MC3E: Further improvements and comparisons between Goddard microphysics schemes and observations, Journal of Geophysical Research: Atmospheres, 121, 1278–1305, 2016.

Testud, J., Le Bouar, E., Obligis, E., and Ali-Mehenni, M.: The rain profiling algorithm applied to polarimetric weather radar, Journal of Atmospheric and Oceanic Technology, 17, 332–356, 2000.

Tiedtke, M.: A comprehensive mass flux scheme for cumulus parameterization in large-scale models, Monthly weather review, 117, 1779–1800, 1989.

Trömel, S., Kumjian, M. R., Ryzhkov, A. V., Simmer, C., and Diederich, M.: Backscatter differential phase—Estimation and variability, Journal of applied meteorology and climatology, 52, 2529–2548, 2013.

Trömel, S., Ryzhkov, A. V., Hickman, B., Mühlbauer, K., and Simmer, C.: Polarimetric Radar Variables in the Layers of Melting and Dendritic Growth at X Band—Implications for a Nowcasting Strategy in Stratiform Rain, Journal of Applied Meteorology and Climatology, 58, 2497—-2522, 2019.

Trömel, S., Simmer, C., Blahak, U., Blanke, A., Ewald, F., Frech, M., Gergely, M., Hagen, M., Hörnig, S., Janjic, T., Kalesse, H., Kneifel, S., Knote, C., Mendrok, J., Moser, M., Möller, G., Mühlbauer, K., Myagkov, A., Pejcic, V., Seifert, P., Shrestha, P., Teisseire, A., von Terzi, L., Tetoni, E., Vogl, T., Voigt, C., Zeng, Y., Zinner, T., and Quaas, J.: Overview: Fusion of Radar Polarimetry and Numerical Atmospheric Modelling Towards an Improved Understanding of Cloud and Precipitation Processes, Atmospheric Chemistry and Physics Discussions, 2021, 1–36, https://doi.org/10.5194/acp-2021-346, 2021.

Uebel, M., Herbst, M., and Bott, A.: Mesoscale simulations of atmospheric CO2 variations using a high-resolution model system with process-based CO2 fluxes, Quarterly Journal of the Royal Meteorological Society, 143, 1860–1876, 2017.

https://doi.org/10.5194/acp-2021-404
Preprint. Discussion started: 15 June 2021

Atmospheric Chemistry and Physics Discussions

van Lier-Walqui, M., Fridlind, A. M., Ackerman, A. S., Collis, S., Helmus, J., MacGorman, D. R., North, K., Kollias, P., and Posselt, D. J.: On polarimetric radar signatures of deep convection for model evaluation: Columns of specific differential phase observed during MC3E, Monthly weather review, 144, 737–758, 2016.

Wicker, L. J. and Skamarock, W. C.: Time-splitting methods for elastic models using forward time schemes, Monthly weather review, 130, 2088–2097, 2002.

Williams, E., Hood, K., Smalley, D., Donovan, M., Melnikov, V., Forsyth, D., Zrnic, D., Burgess, D., Douglas, M., Sandifer, J., et al.: End-to-end calibration of NEXRAD differential reflectivity with metal spheres, in: Proc. 36th Conf. Radar Meteorol, 2013.

Xie, X., Evaristo, R., Troemel, S., Saavedra, P., Simmer, C., and Ryzhkov, A.: Radar Observation of Evaporation and Implications for Quantitative Precipitation and Cooling Rate Estimation, Journal of Atmospheric and Oceanic Technology, 33, 1779–1792, https://doi.org/10.1175/JTECH-D-15-0244.1, 2016.

Xie, X., Shrestha, P., Mendrok, J., Carlin, J., Trömel, S., and Blahak, U.: Bonn Polarimetric Radar forward Operator (B-PRO), https://www.tr32db.uni-koeln.de/search/view.php?doiID=115, [Accessed 15. April 2021], 2021.

Yuter, S. E. and Houze Jr, R. A.: Three-dimensional kinematic and microphysical evolution of Florida cumulonimbus. Part II: Frequency distributions of vertical velocity, reflectivity, and differential reflectivity, Monthly weather review, 123, 1941–1963, 1995.

Zängl, G., Reinert, D., Rípodas, P., and Baldauf, M.: The ICON (ICOsahedral Non-hydrostatic) modelling framework of DWD and MPI-M: Description of the non-hydrostatic dynamical core, Quarterly Journal of the Royal Meteorological Society, 141, 563–579, 2015.

Zeng, Y., Blahak, U., and Jerger, D.: An efficient modular volume-scanning radar forward operator for NWP models: description and coupling to the COSMO model, Quarterly Journal of the Royal Meteorological Society, 142, 3234–3256, 2016.

Zrnic, D. S. and Ryzhkov, A. V.: Polarimetry for weather surveillance radars, Bulletin of the American Meteorological Society, 80, 389–406, 1999.

https://doi.org/10.5194/acp-2021-404
Preprint. Discussion started: 15 June 2021

Atmospheric Chemistry and Physics Discussions

FIGURES

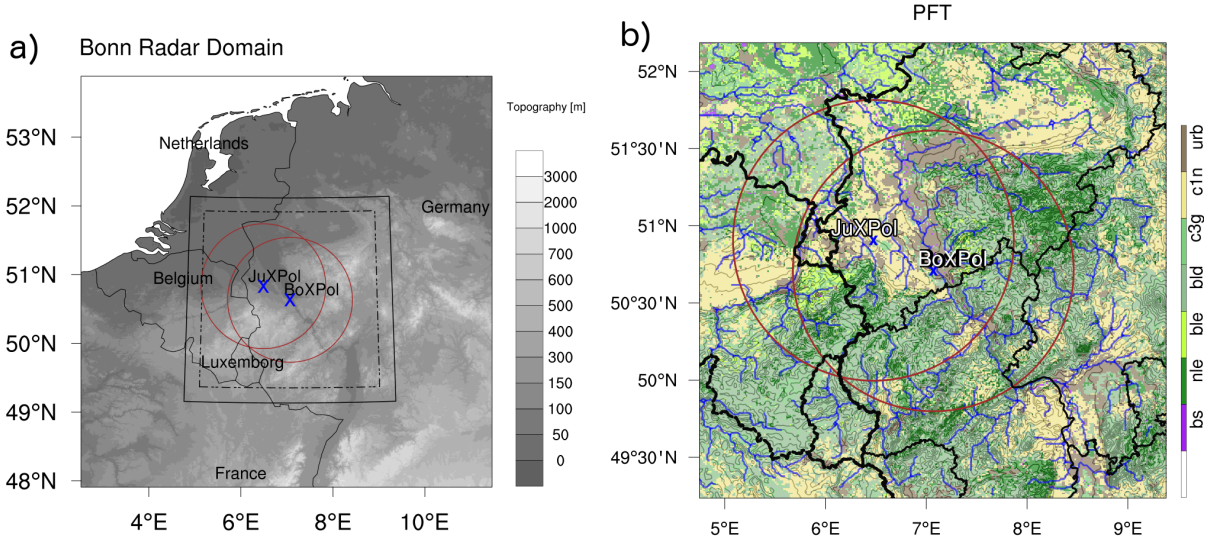

Figure 1. a) Spatial pattern of topography and extent of Bonn Radar domain (solid line) including the coverage of BoXPol and JuXPol (red circles). The dotted lines indicate the inner domain (excluding the relaxation zone) used to compute the domain average precipitation. b) Spatial pattern of plant functional types (PFTs). Also shown is the coverage of two X-band radars.

https://doi.org/10.5194/acp-2021-404
Preprint. Discussion started: 15 June 2021

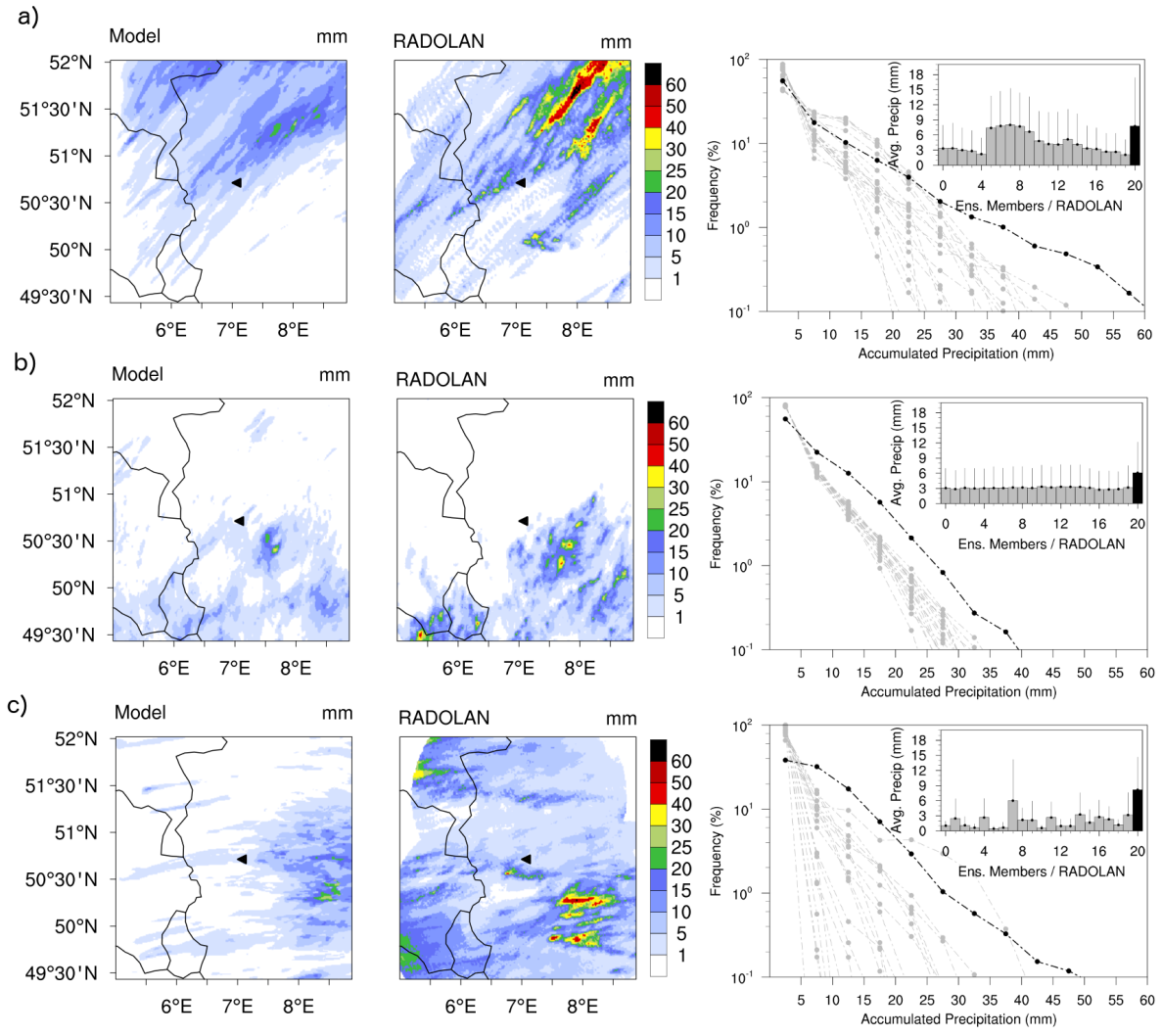

Figure 2. Spatial pattern and frequency distribution of accumulated precipitation over the Bonn Radar domain for three case studies (a,b and c). For each case studies, the left and middle panel shows the spatial pattern of accumulated precipitation from model and observations. For model, the spatial pattern of ensemble average is shown. The right panel shows the frequency distribution of accumulated precipitation, including the domain average accumulated precipitation and 1 standard deviation for the different ensemble member and the observation in the inset.

https://doi.org/10.5194/acp-2021-404
Preprint. Discussion started: 15 June 2021

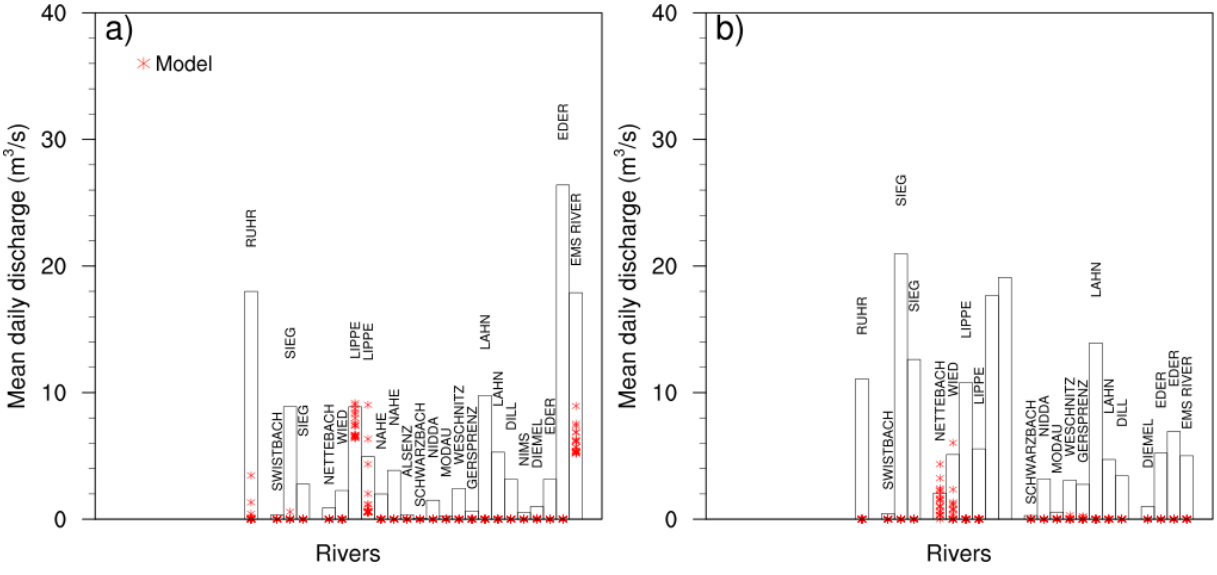

Figure 3. Daily discharge comparison of model ensemble members with available data from GRDC for first and second test case. Discharge data was not available to compare for the third test case.

https://doi.org/10.5194/acp-2021-404
Preprint. Discussion started: 15 June 2021

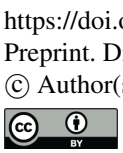

Atmospheric Chemistry and Physics Discussions

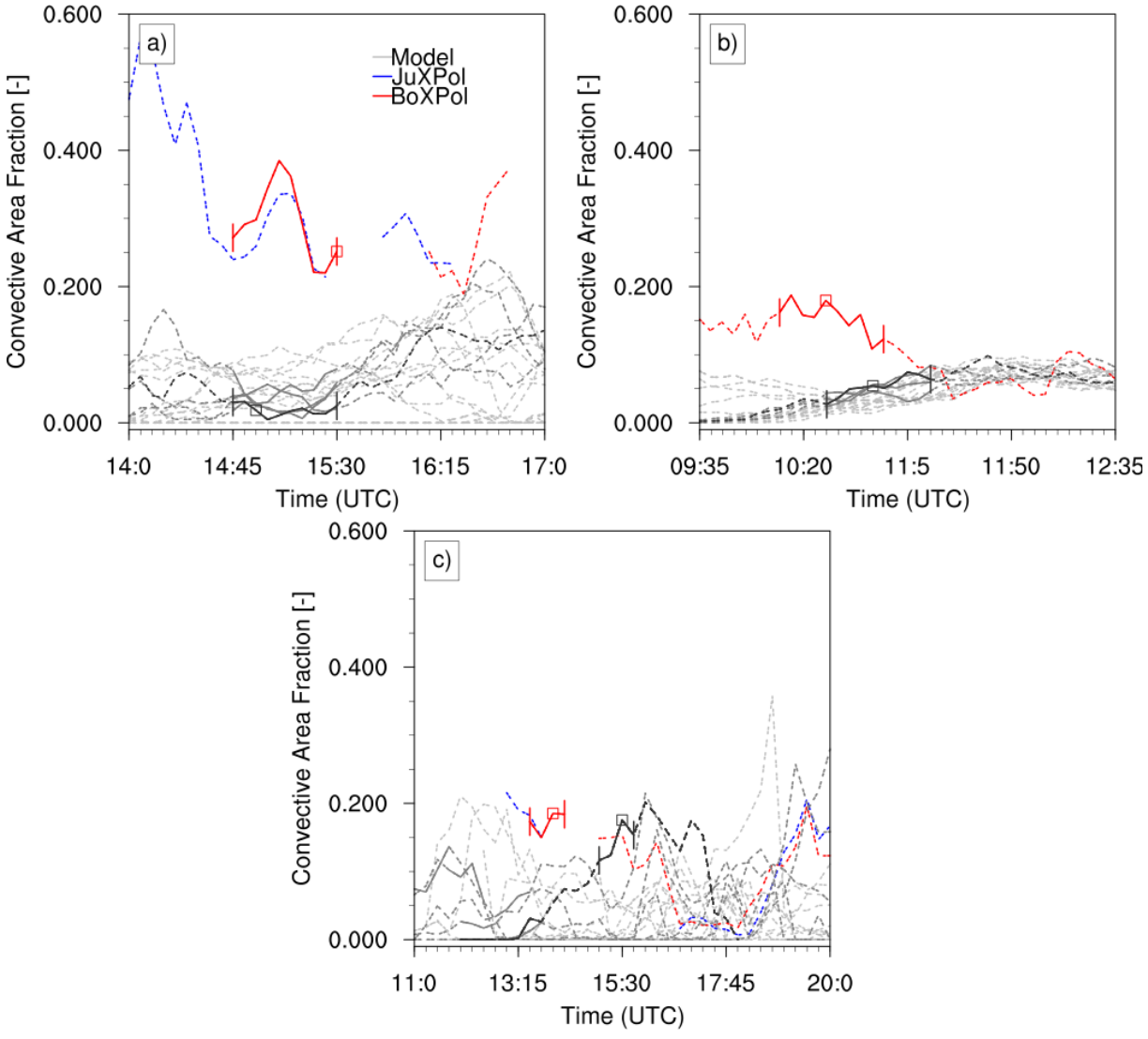

Figure 4. Convective Area Fraction (CAF) of model ensemble members and observations for the three different case studies. The CAF time-series with solid lines are used for CFAD comparison. The model ensemble member with black color is also used for polarimetric signature comparison. The square marker represents the snapshot used for polarimetric comparision for each case study. The observations from BoXPol or JuXPol are shown upon coverage and data availability. The gaps in the radar data represents times, when the polarimetric signatures are strongly attenuated or if the storm extent is only partially covered by the radar.

https://doi.org/10.5194/acp-2021-404
Preprint. Discussion started: 15 June 2021

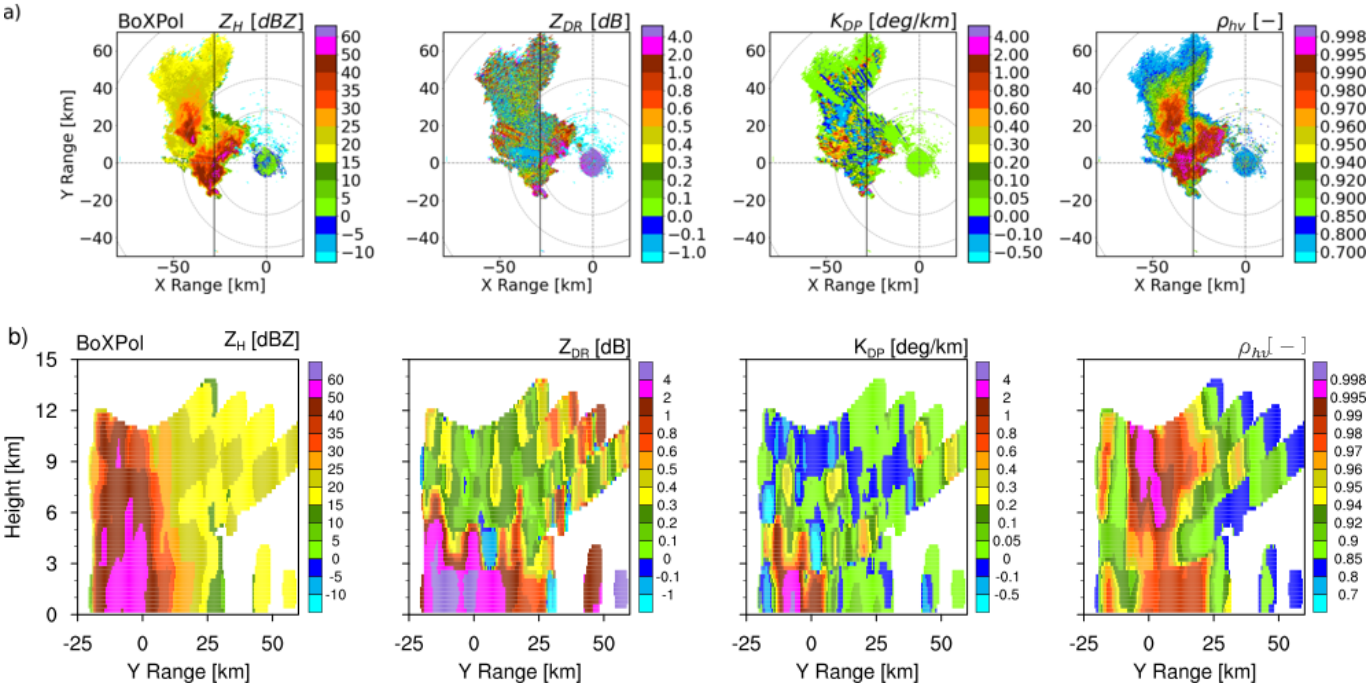

Figure 5. a) Plan position indicator (PPI) plots of horizontal reflectivity, differential reflectivity, sp. differential phase and cross-correlation coefficient at 8.2 degree elevation measured by BoXPol on 5 July 2015 at 1530 UTC. The dotted contours represent slant ranges associated with heights of 1 , 4.5 and 7 km. b) Cross-section of the same polarimetric variables from the gridded data. The vertical line in a) indicates the location of cross-section plots.

https://doi.org/10.5194/acp-2021-404
Preprint. Discussion started: 15 June 2021

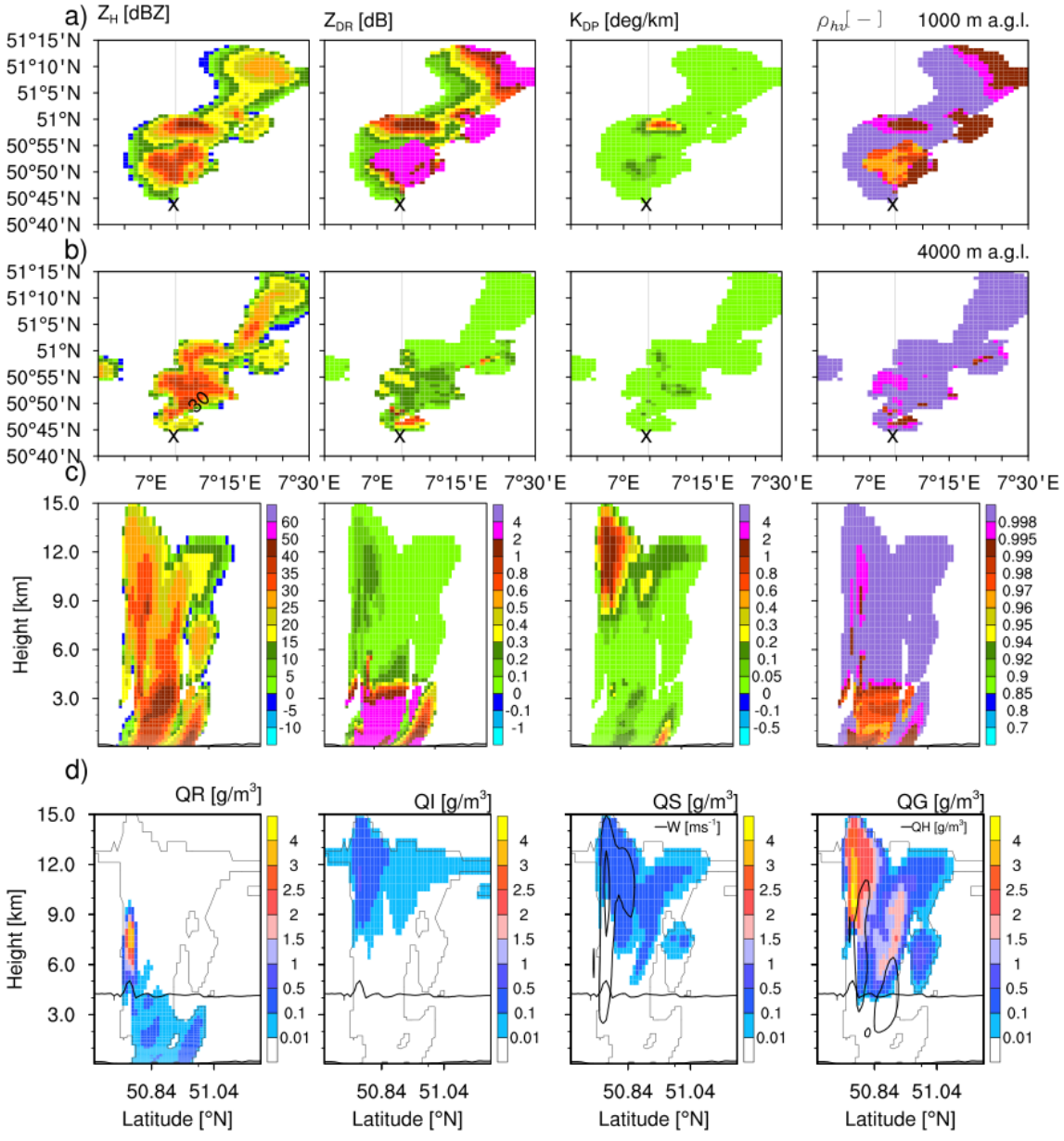

Figure 6. a,b) Model simulated horizontal reflectivity, differential reflectivity, sp. differential phase and cross-correlation coefficient at low level (1000 m a.g.l.) and near melting layer (4000 m a.g.l.) on 5 July 2015 at 1455 UTC. c) Cross-section of the same polarimetric variables. d) Cross-section of model simulated hydrometeors. Also shown are the $0^{\circ}C$ line (solid black line), contours of vertical velocity [5, 40 m/s] with QS and contours of hail mixing ratio with QG. The vertical line in a,b) indicates the location of cross-section plots. The 'x' mark refers to the BoXPol location.

https://doi.org/10.5194/acp-2021-404
Preprint. Discussion started: 15 June 2021

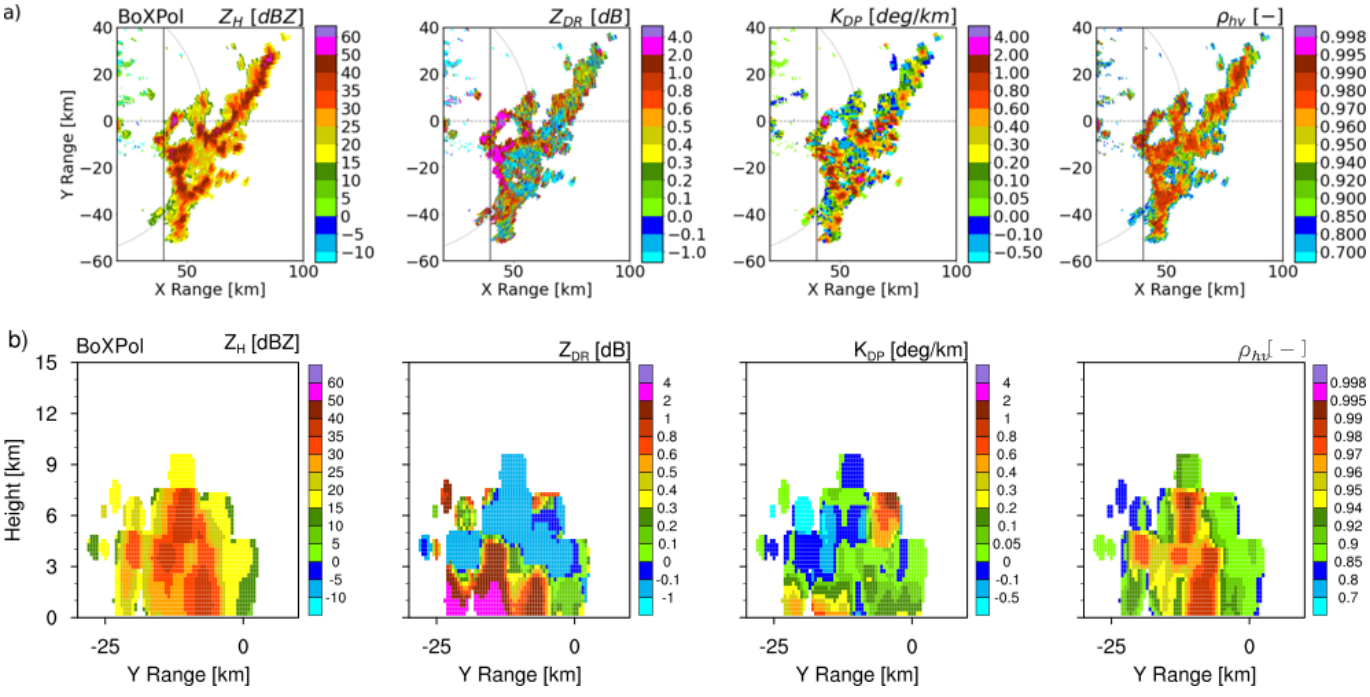

Figure 7. a) Plan position indicator (PPI) plots of horizontal reflectivity, differential reflectivity, sp. differential phase and cross-correlation coefficient at 1.0 degree elevation measured by BoXPol on 13 May 2016 at 1030 UTC. The dotted contours represent slant ranges associated with height of 1 km. b) Cross-section of the same polarimetric variables from the gridded data. The vertical line in a) indicates the location of cross-section plots.

https://doi.org/10.5194/acp-2021-404
Preprint. Discussion started: 15 June 2021

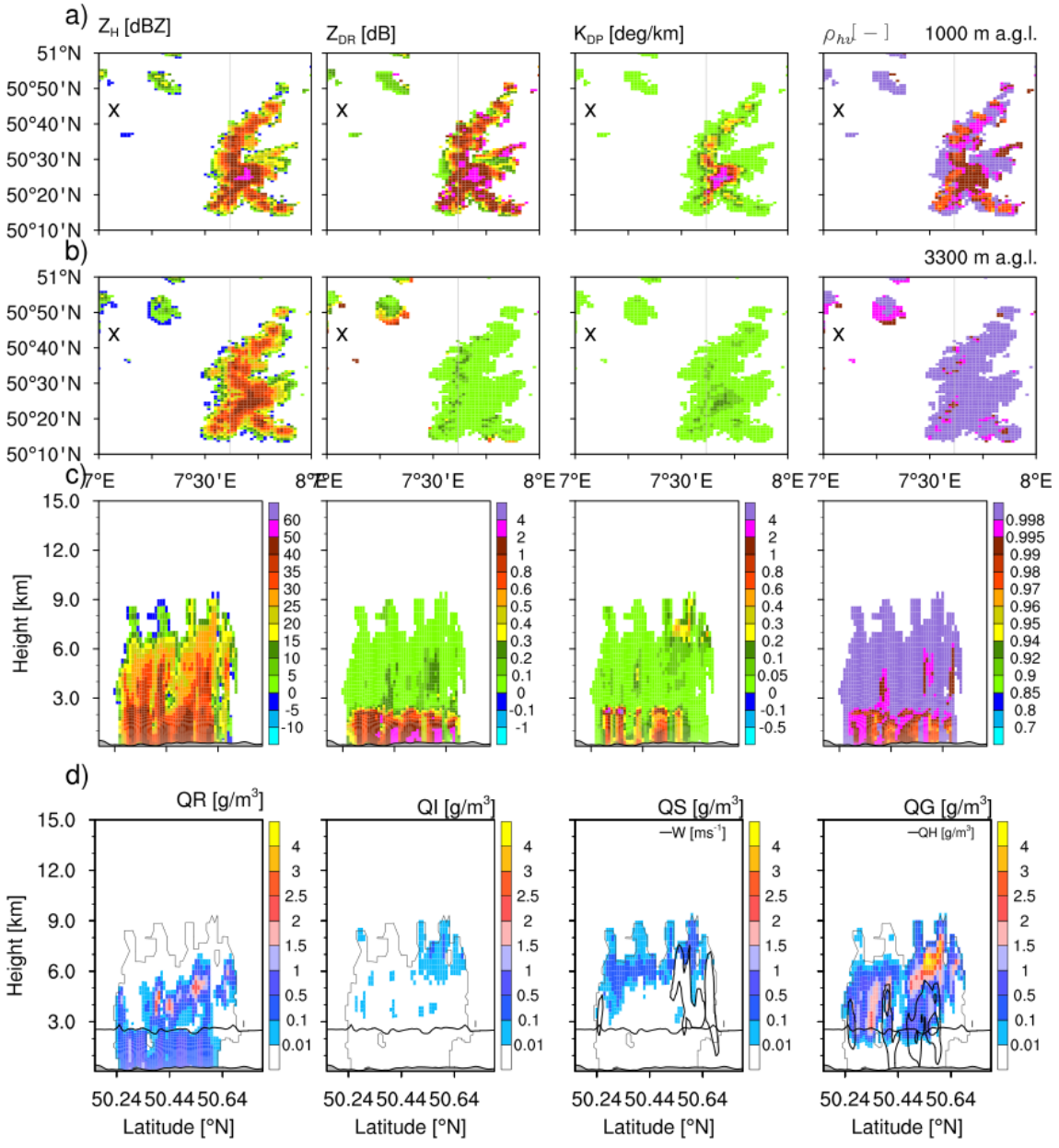

Figure 8. a,b) Model simulated horizontal reflectivity, differential reflectivity, sp. differential phase and cross-correlation coefficient at low level (1000 m a.g.l.) and near melting layer (3300 m a.g.l.) on 13 May 2016 at 1050 UTC. c) Cross-section of the same polarimetric variables. d) Cross-section of model simulated hydrometeors. Also shown are the $0^{\circ}C$ line (solid black line), contours of vertical velocity [5, 40 m/s] with QS and contours of hail mixing ratio with QG. The vertical line in a,b) indicates the location of cross-section plots. The 'x' mark refers to the BoXPol location.

https://doi.org/10.5194/acp-2021-404
Preprint. Discussion started: 15 June 2021

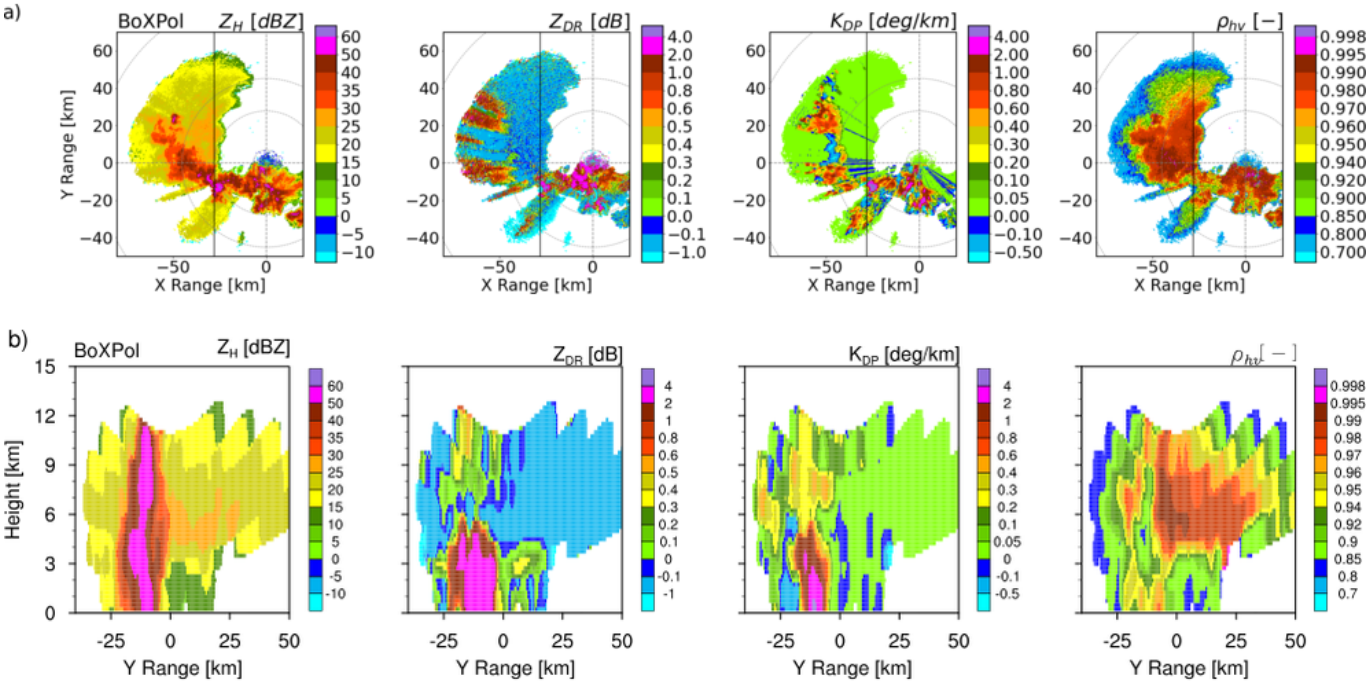

Figure 9. a) Plan position indicator (PPI) plots of horizontal reflectivity, differential reflectivity, sp. differential phase and cross-correlation coefficient at 8.2 degree elevation measured by BoXPol on 6 July 2017 at 1400 UTC. The dotted contours represent slant ranges associated with height of 1, 4, 6.5 and 13 km. b) Cross-section of the same polarimetric variables from the gridded data. The vertical line in a) indicates the location of cross-section plots.

https://doi.org/10.5194/acp-2021-404
Preprint. Discussion started: 15 June 2021

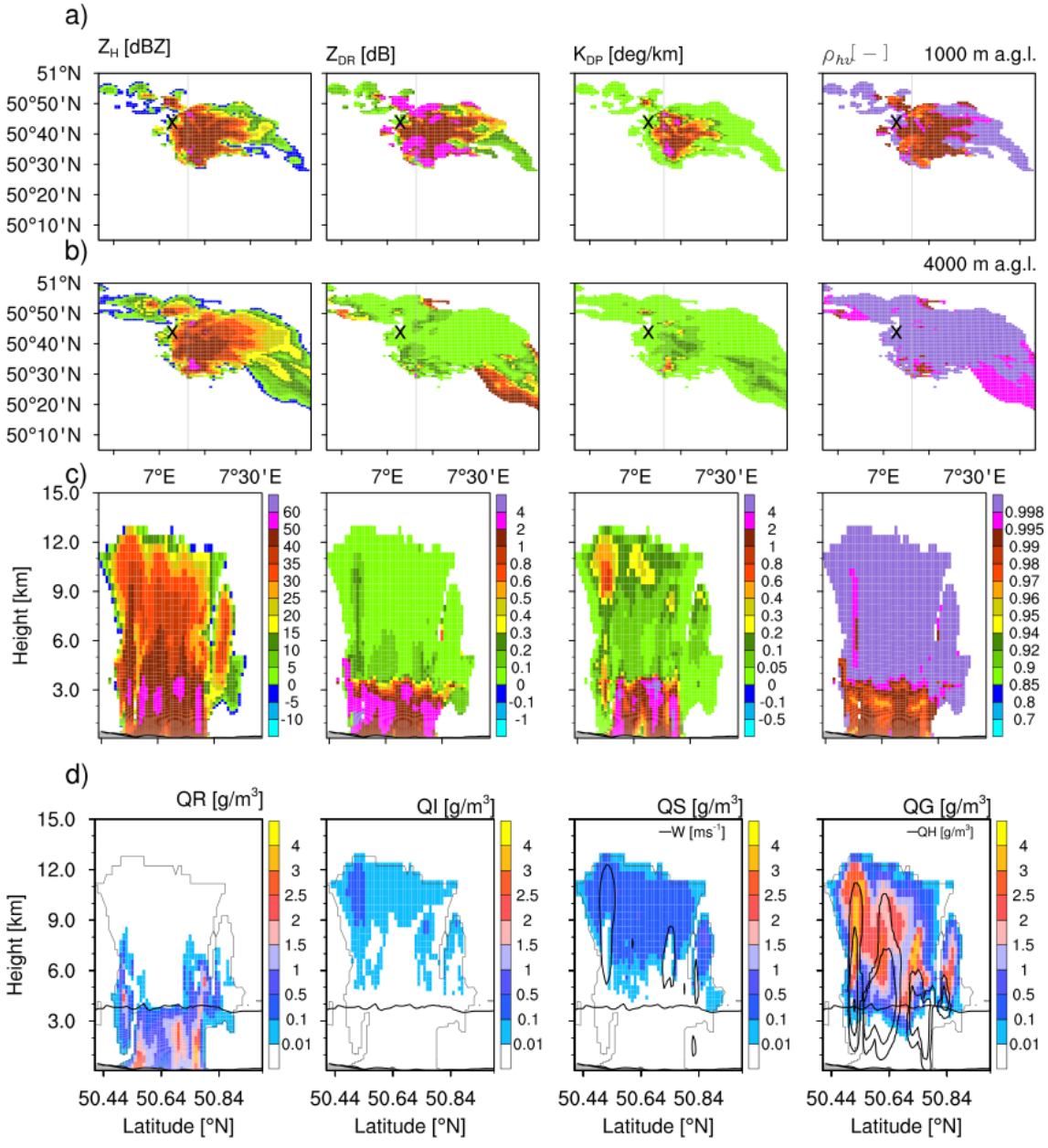

Figure 10. a,b) Model simulated horizontal reflectivity, differential reflectivity, sp. differential phase and cross-correlation coefficient at low level (1000 m a.g.l.) and near melting layer (4000 m a.g.l.) on 6 July 2017 at 1530 UTC. c) Cross-section of the same polarimetric variables. d) Cross-section of model simulated hydrometeors. Also shown are the $0^{\circ}C$ line (solid black line), contours of vertical velocity [5, 40 m/s] with QS and contours of hail mixing ratio with QG. The vertical line in a,b) indicates the location of cross-section plots. The 'x' mark refers to the BoXPol location.

https://doi.org/10.5194/acp-2021-404
Preprint. Discussion started: 15 June 2021

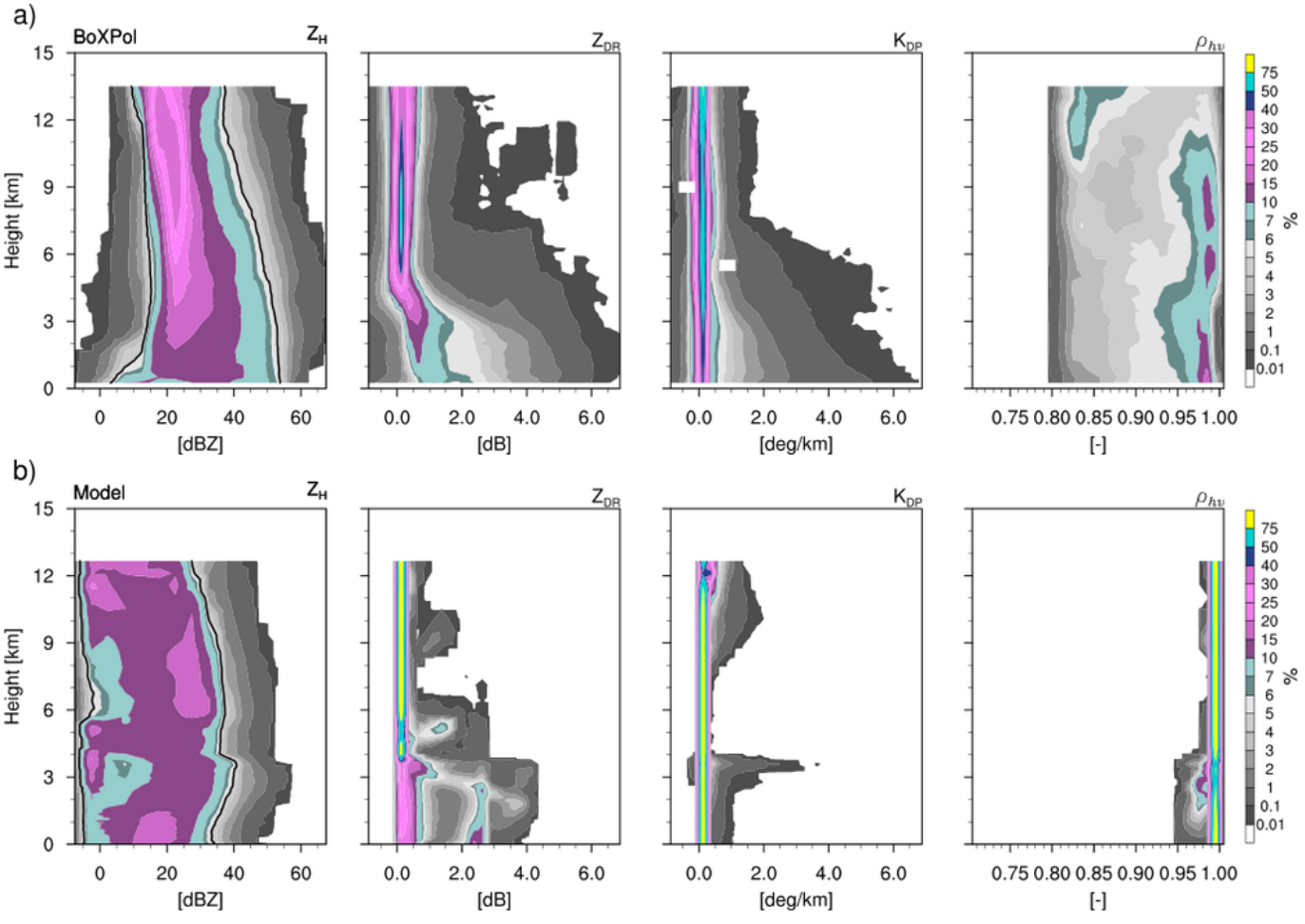

Figure 11. Contoured frequency altitude diagrams (CFADs) of horizontal reflectivity, differential reflectivity, sp. differential phase and cross-correlation coefficient from 1445 to 1530 UTC on 5 July 2015. CFADs from the model are shown for 5 ensemble members.

https://doi.org/10.5194/acp-2021-404
Preprint. Discussion started: 15 June 2021

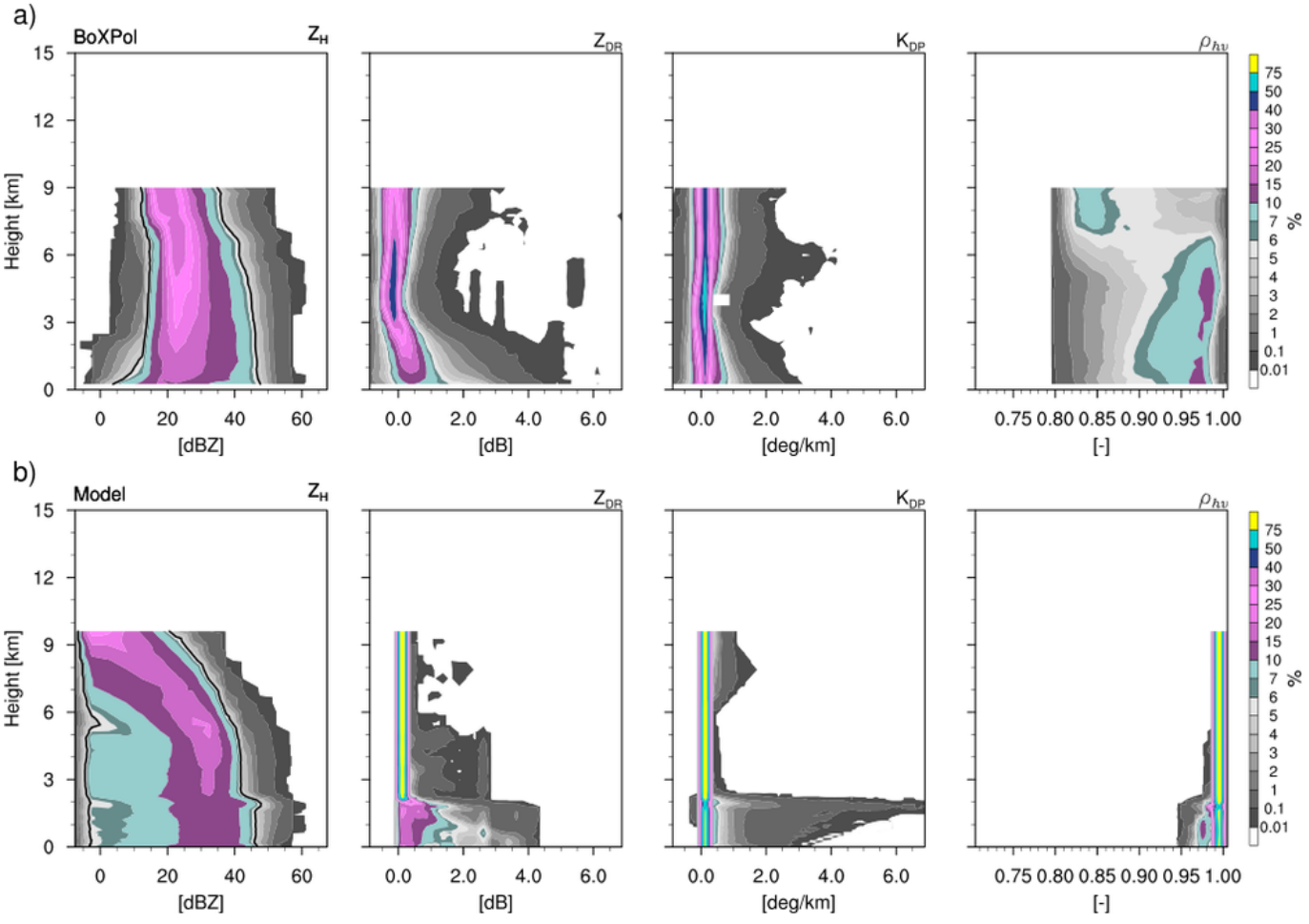

Figure 12. Contoured frequency altitude diagrams (CFADs) of horizontal reflectivity, differential reflectivity, sp. differential phase and cross-correlation coefficient from 1010 to 1055 UTC on 13 May 2016. CFADs from the model are shown for 5 ensemble members from 10:30-11:15 UTC.

https://doi.org/10.5194/acp-2021-404
Preprint. Discussion started: 15 June 2021

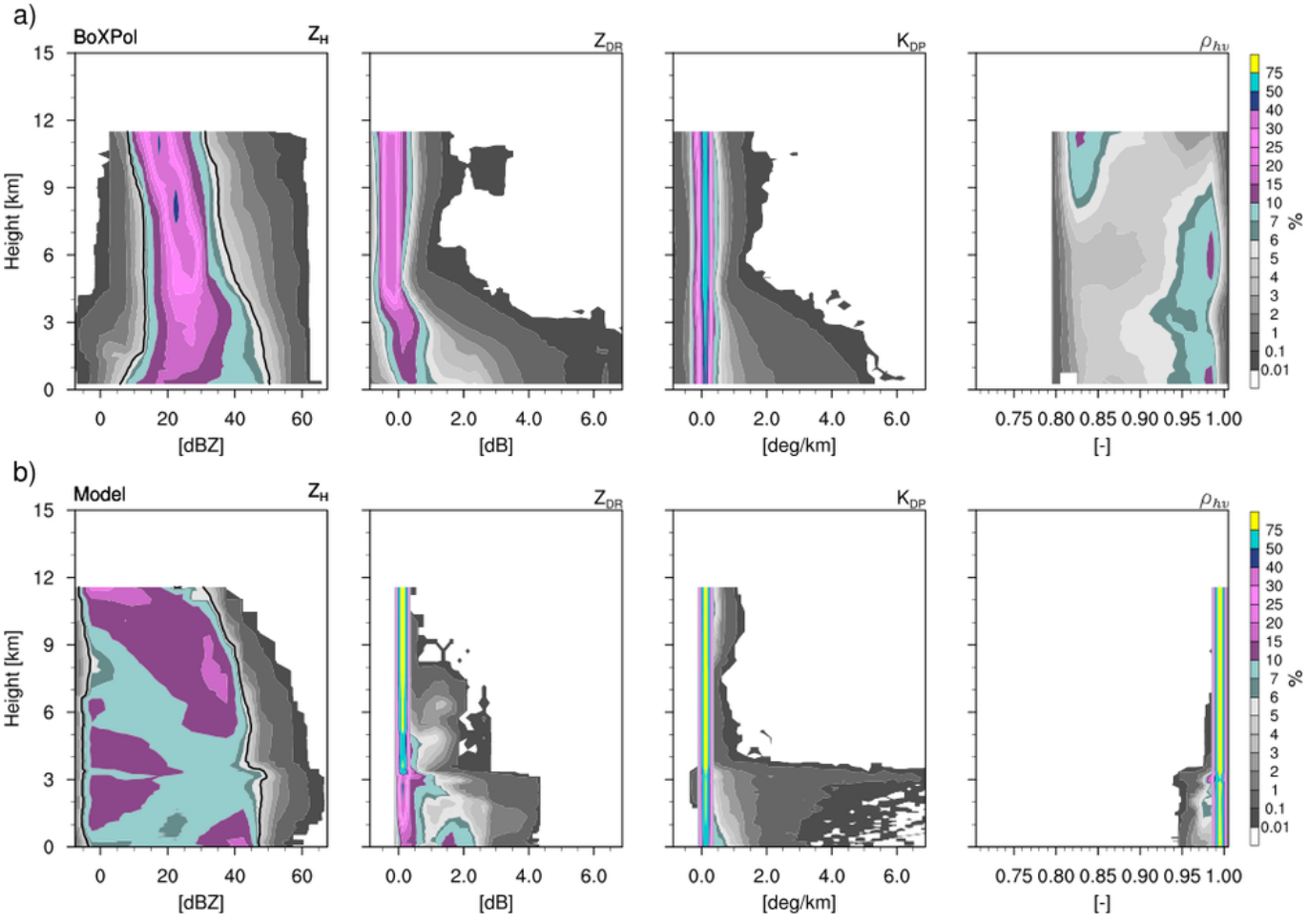

Figure 13. Contoured frequency altitude diagrams (CFADs) of horizontal reflectivity, differential reflectivity, sp. differential phase and cross-correlation coefficient from 1330 to 1415 UTC on 13 May 2016. CFADs from the model are shown for 1 ensemble member from 1500 to 1545 UTC.

https://doi.org/10.5194/acp-2021-404
Preprint. Discussion started: 15 June 2021

Atmospheric Chemistry and Physics Discussions

TABLES

Table 1. Hydrometeor parameters for mass-diameter relationship and generalized gamma distribution for the of 2-moment microphysics scheme including minimum and maximum values of mean particle mass.

Hydrometeors	a (mkg^{-b})	b	ν	μ	x_{min} (kg)	x_{max} (kg)
cloud	0.124	1/3	0.0	1/3	4.20×10^{-15}	2.60×10^{-10}
rain	0.124	1/3	0.0	1/3	2.60×10^{-10}	3.00×10^{-6}
ice	0.835	0.39	0.0	1/3	1.00×10^{-12}	1.00×10^{-6}
snow	2.4	0.455	0.0	0.50	1.00×10^{-10}	2.00×10^{-5}
graupel	0.142	0.314	1.0	1/3	1.00×10^{-9}	5.00×10^{-4}
hail	0.1366	1/3	1.0	1/3	2.60×10^{-9}	5.00×10^{-4}

https://doi.org/10.5194/acp-2021-404
Preprint. Discussion started: 15 June 2021

Atmospheric Chemistry and Physics Discussions

Table 2. Large-scale continental aerosol specification for cloud droplet nucleation and default parameters for ice nucleation.

	N_{CN}, m^{-3}	$R2, \mu m$	$log(\sigma_s)$	ϵ_s	$N_{x=d}, m^{-3}$	$N_{x=s}, m^{-3}$	$N_{x=o}, m^{-3}$
CD^1	1700×10^6	0.03	0.2	0.7	162×10^3	15×10^6	177×10^6

https://doi.org/10.5194/acp-2021-404
Preprint. Discussion started: 15 June 2021

Atmospheric Chemistry and Physics Discussions

Table 3. Assumed hydrometeor physical properties for T-matrix computation in the B-PRO

	D_x	AR	σ_c
Rain	50 μm-8 mm	(Brandes et al., 2002)	10°
Cloud ice	20 μm- 0.5 mm	$\sim 0.2, plates$ (Andrić et al., 2013)	12°
Snow	50 μm – 20 mm	$0.7 - 0.2 \times D_x/D_{x,max}$ (Xie et al., 2016)	40°
Graupel	50 μm – 30 mm	$max(1.0 - 20 \times D_x, 0.8)$ (Ryzhkov et al., 2011)	40°
Hail	50 μm – 30 mm	$max(1.0 - 20 \times D_x, 0.8)$ (Ryzhkov et al., 2011)	40°